Multiscale modelling of drug transport and metabolism in liver spheroids

Joseph A. Leedale[1*], Jonathan A. Kyffin[2], Amy L. Harding[3], Helen E. Colley[3], Craig Murdoch[3], Parveen Sharma[4], Dominic P. Williams[5], Steven D. Webb[1,2], Rachel N. Bearon[1]

[1]EPSRC Liverpool Centre for Mathematics in Healthcare, Dept. of Mathematical Sciences, University of Liverpool, Liverpool, L69 7ZL, UK

[2]Dept. of Applied Mathematics, Liverpool John Moores University, Liverpool, L3 3AF, UK

[3]School of Clinical Dentistry, University of Sheffield, Claremont Crescent, Sheffield, S10 2TA, UK

[4]MRC Centre for Drug Safety Science, Dept. of Molecular and Clinical Pharmacology, University of Liverpool, Liverpool, L69 3GE, UK

[5]AstraZeneca, IMED Biotech Unit, Drug safety & Metabolism, Cambridge Science Park, Cambridge, CB4 0FZ, UK

*Correspondence

Dr Joseph Leedale
Dept. of Mathematical Sciences
University of Liverpool
Liverpool L69 7ZL
United Kingdom
Tel: +44 (0)151 794 4049
Email: j.leedale@liverpool.ac.uk

Abstract

In early preclinical drug development, potential candidates are tested in the laboratory using isolated cells. These *in-vitro* experiments traditionally involve cells cultured in a two-dimensional monolayer environment. However, cells cultured in three-dimensional spheroid systems have been shown to more closely resemble the functionality and morphology of cells *in-vivo*. While the increasing usage of hepatic spheroid cultures allows for more relevant experimentation in a more realistic biological environment, the underlying physical processes of drug transport, uptake and metabolism contributing to the spatial distribution of drugs in these spheroids remain poorly understood. The development of a multiscale mathematical modelling framework describing the spatiotemporal dynamics of drugs in multicellular environments enables mechanistic insight into the behaviour of these systems. Here, our analysis of cell membrane permeation and porosity throughout the spheroid reveals the impact of these properties on drug penetration, with maximal disparity between zonal metabolism rates occurring for drugs of intermediate lipophilicity. Our research shows how mathematical models can be used to simulate the activity and transport of drugs in hepatic spheroids, and in principle any organoid, with the ultimate aim of better informing experimentalists on how to regulate dosing and culture conditions to more effectively optimise drug delivery.

Keywords: Drug transport; Spheroid; Organoid; Hepatocytes; Systems pharmacology; Mathematical modelling.

1   Introduction

The discovery of potential toxicity *in-vitro* remains an important process in providing pre-clinical safety assurances during drug development. However, conventional 2D *in-vitro* experiments, such as monolayer cell culture, tend to be poorly predictive of toxicity, and emerging 3D systems are shown to be more physiologically relevant and predictive of the *in-vivo* environment (1, 2). Accordingly, 3D cell culture systems such as multicellular spheroids are increasingly being utilised in drug development and hepatic safety assessment (3, 4). Although 3D spheroid systems offer improvements in terms of physiological relevance and *in-vivo*-like functionality, the mechanistic interaction between these systems and drugs is not yet fully understood.

Multiscale *in-silico* methods can improve the application of 3D spheroid models to assess the hepatotoxicity of drug candidates (5, 6). Indeed, mechanistic mathematical modelling of drug metabolism and transport in 3D microtissues is important for the pharmaceutical industry as it facilitates an improved platform for both preclinical drug development and *in-vivo* extrapolation (7). This utilisation of mathematical models, devised to tackle pharmacological research challenges in a systems biology approach, has become known as part of the evolving field(s) of systems pharmacology and/or systems toxicology (8, 9). This approach is a multiscale, multidisciplinary field that employs holistic, integrative methods in order to enhance the understanding and prediction of emergent system properties. Moreover, this methodology is strictly quantitative requiring the integration of quantitative data and modelling to develop mechanistic knowledge of the system and reveal pharmacological and toxicological properties. Consequently, systems pharmacology models are becoming an increasingly

important part of the toolkit to improve capabilities and drive innovation for *in-vitro* safety assessment (10-12).

In this study we have characterised the spatiotemporal dynamics of drugs in an *in-vitro* hepatic spheroid system by simulating relevant physical processes *in-silico*. A data-driven, multiscale, mathematical modelling framework combining mechanistic information relating to the diffusion, transport and metabolism of chemical species in a hepatocyte spheroid is presented. A microscale single-cell model is analysed to study different transport mechanisms by varying boundary conditions on the cell membrane. This model is then coupled to a multicellular model developed to evaluate the effects of cellular arrangement and density on the transport and penetration of drugs, simulating the *in-vitro* microtissue environment. Such effects include a non-linear relationship between drug lipophilicity and spheroid penetration whereby drug delivery to the spheroid core is minimised for drugs of intermediate lipophilicity. The integration of experimental data allows for the development of realistic geometries and parameterisation of the multiscale model for a range of drugs. Ultimately, by accurately simulating the processes of drug transport and metabolism we aim to enhance the understanding of underlying mechanisms and optimise the use of these systems *in-vitro*.

2   Methods

2.1   Microscale transport – crossing the cell membrane

To simulate the distribution of drugs throughout a 3D tissue comprised of multiple hepatocytes, it is necessary to determine how drugs penetrate and cross the cell membrane. This membrane comprises a phospholipid bilayer, providing a hydrophobic protective barrier for the cell.

4

Consequently, this chemical barrier property is a key determinant in the effective permeability of any drug. Many factors affect drug permeability in tissues such as ionisation, aqueous diffusion between lipid barriers, and protein binding, but the partition into the membrane (determined by lipid solubility) is one of the most important (13). Highly lipophilic substances can more readily penetrate the membrane via free diffusion, whilst relatively hydrophilic substances, (highly soluble in polar solvents such as water or blood), cannot enter the cell easily and require specific transporters (Figure 1A). The relative role of transporter proteins in intracellular drug transport is still debated and there remain different views as to whether passive diffusion or carrier-mediated transport is the major mechanism (14-18). For the entirety of this study we refer to the two main types of transport: passive diffusion – entering cells down a concentration gradient directly through the membrane (passive); and carrier-mediated transport – entering cells via specific transporter proteins embedded in the plasma membrane (passive or active).

The mathematical representation of microscale drug transport across a cell membrane can be studied with a simple model considering the processes governing drug concentration dynamics in two phases, inside and outside the cell, with a permeable barrier in-between. Once inside the cell, the drug is removed via metabolism. We assume diffusion occurs at different rates inside (D_I) and outside (D_E) of the cell, which we initially assume is spherical of radius R, but relax this assumption in section 2.3. The drug concentration (C) dynamics inside the cell are given by the partial differential equation (PDE):

$$\frac{\partial C}{\partial t} = D_I \nabla^2 C - \frac{V_{max} C}{C + K_m} \, , \tag{1}$$

where V_{max} is the maximum metabolic rate and K_m represents the drug concentration at which metabolism is half maximal. Since there is no flow within the *in vitro* system, and the dominant form of removal within the multiscale model is assumed to be due to intracellular metabolism, we assume that outside the cell drug transport is governed by diffusion processes only:

$$\frac{\partial C}{\partial t} = D_E \nabla^2 C \ . \tag{2}$$

For simplicity, we assume that the problem is radially symmetric and rescale the model with respect to cell radius and internal diffusion time (such that the cell boundary is now given by $r = 1$) to give

$$\frac{\partial C}{\partial t} = \frac{1}{r^2}\frac{\partial}{\partial r}\left(r^2 \frac{\partial C}{\partial r}\right) - \frac{V_{max}C}{C + K_m}, \qquad r \leq 1, \tag{3}$$

$$\frac{\partial C}{\partial t} = \frac{D}{r^2}\frac{\partial}{\partial r}\left(r^2 \frac{\partial C}{\partial r}\right), \qquad r > 1, \tag{4}$$

where $D = D_E/D_I$ due to rescaling (see supplementary material for details). We impose the following boundary conditions at the cell centre ($r = 0$), for radial symmetry, and a distance away from the cell ($r = r_{max}$):

$$\frac{\partial C}{\partial r} = 0\ , \qquad r = 0\ , \tag{5}$$

$$C = C_{r_{max}}\ , \qquad r = r_{max}\ , \tag{6}$$

where $C_{r_{max}}$ is a constant supply term. Assume that the flux at the cell boundary is equal such that mass is conserved, i.e.,

$$D_I \frac{\partial C_I}{\partial r} = D_E \frac{\partial C_E}{\partial r}\ , \qquad r = 1\ , \tag{7}$$

6

where C_I and C_E are used to distinguish between interior and exterior drug concentrations at the cell membrane boundary. A further boundary condition must be specified at the cell membrane boundary in order to solve the coupled PDE system and investigate the effects of different means of drug transport.

2.1.1 Passive diffusion

The following boundary condition is imposed to describe the flux of drug into the cell due to passive diffusion:

$$D_I \frac{\partial C_I}{\partial r} = D_E \frac{\partial C_E}{\partial r} = Q(C_E - C_I) , \qquad r = 1 , \qquad (8)$$

where Q is the permeability coefficient. The mathematical model can be solved numerically in MATLAB R2017b. For methodological details regarding derivations, numerical solutions and simulations of microscale transport, see the supplementary material.

The impact of the permeability coefficient, Q, on the steady-state distribution of drug concentration can be seen in Figure 1B (for temporal dynamics, see supplementary animations). For low permeability coefficients ($Q \ll 1$), there is less drug penetration per unit time and so there is a low steady-state value inside the cell and a large discontinuity at the cell membrane. As Q increases, relatively more drug enters the cell per unit time and in the limit, as $Q \to \infty$, the steady-state solutions converge such that the drug concentration profile is continuous ($C_E = C_I$) at the cell membrane boundary (which now provides no effective barrier or resistance) and the steady-state profile represents the balance of supply via diffusion and removal via intracellular metabolism.

2.1.2 Carrier-mediated transport

For drugs whose physicochemical properties prohibit direct permeation across the cell membrane, specific transporter proteins are required that can mediate the transfer process. The reliance on transporter (or carrier) proteins dictates that the flux is now saturable with an explicit dependence on the surface area concentration, binding affinities, and activity of transporters in the cell membrane. In this scenario, the boundary condition representing membrane transport cannot be sufficiently represented by the passive diffusion condition in equation (8) and so we implement a simple carrier model as applied in other similar physiological membrane transport models, e.g., Keener & Sneyd (19) and Wood & Whitaker (20). This carrier model can be applied to define the flux boundary condition for the carrier-mediated transport model scenario:

$$D_I \frac{\partial C_I}{\partial r} = \frac{T_0(C_E - \alpha_1 C_I)}{\alpha_2 + \alpha_3 C_E + \alpha_4 C_I + \alpha_5 C_E C_I} \, , \qquad r = 1 \, , \qquad (9)$$

where T_0 represents transporter protein concentration on the cell membrane and $\alpha_1, \alpha_2, \alpha_3, \alpha_4, \alpha_5$ represent algebraic expressions dependent on kinetic rates in the carrier model such as binding rates (see supplementary material for more information).

The barrier effect provided by the carrier-mediated transport of drugs across the cell membrane allows for a discontinuity in the steady-state profile of the drug concentration distribution when there is a constant external supply that diffuses towards a metabolically active cell (as before with the passive diffusion case with low permeability). Indeed the carrier mediated transport condition can be reduced to the passive diffusion condition mathematically with appropriate parametrisation (e.g., $T_0 = Q, \alpha_{1,2} = 1, \alpha_{3,4,5} = 0$). Furthermore, the flexibility of the carrier-

mediated condition facilitates the implementation of implicit active processes whereby the flux of drug can move uphill against its concentration gradient (e.g., see Figure 1C). This can be achieved with appropriate parameterisation of the simple carrier model such that $\alpha_1 < 1$, e.g. when binding affinity/dissociation in the interior is lower/higher than exterior binding/dissociation.
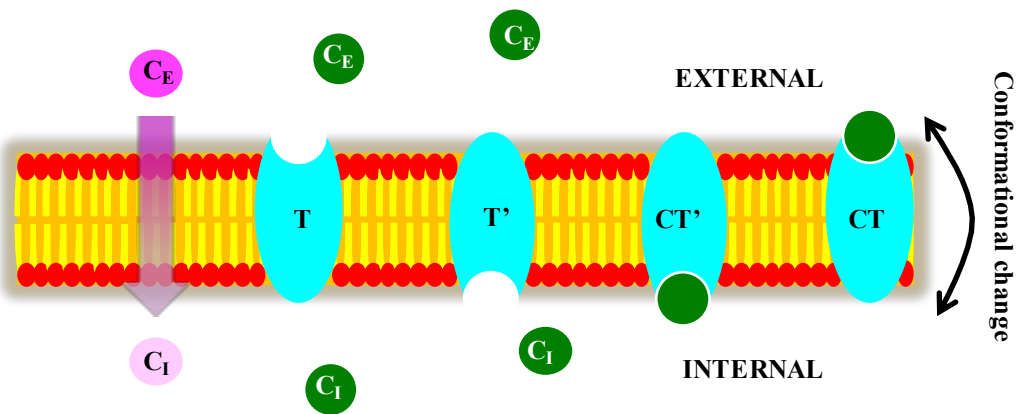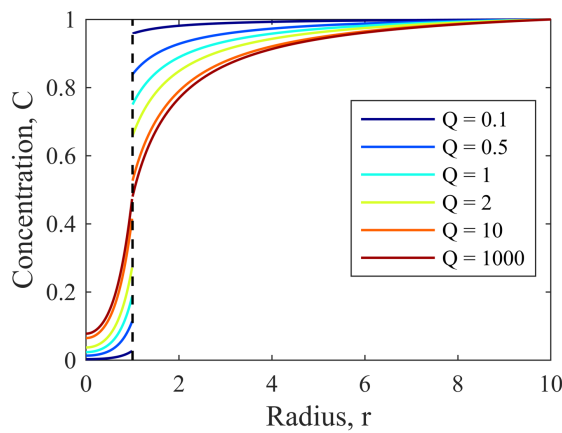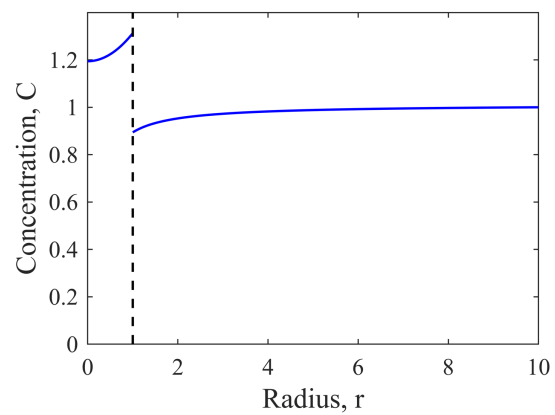

Figure 1: **Modelling transmembrane transport in a single cell.** (A): Drug transport schematics across the cell membrane. Two modes of transport are considered, passive diffusion (pink substrates/circles) and carrier-mediated transport (green substrates/circles). Drugs that permeate the cell via passive diffusion move down a concentration gradient directly through the membrane and are limited by their associated permeability coefficient. This coefficient is dependent on the physicochemical properties of the drug and drugs which cross the membrane via this mechanism are typically small and lipophilic. Other drugs may require the action of specific membrane-bound transporter proteins to enter the cell (carrier-mediated transport). In this study, it is assumed that this mechanism is dependent on carrier proteins/receptors (depicted in cyan) which can reversibly bind to the substrate and undergo conformational changes to transport the substrate across the membrane. Species within the figure are

annotated with symbols related to mathematical models described in the main text and supplementary material. (B): Variation in the permeability coefficient determines the steady-state concentration profile of drug concentration in a single cell for the passive diffusion transport mechanism. Low permeability results in a discontinuity at the cell membrane ($D = 2, V_{max} = 10, K_m = 0.5, C_{r_{max}} = 1$). (C): For specific parameter choices within the carrier-mediated transport model, a steady-state can be reached such that the drug is transported against its concentration gradient, implicitly simulating an active process ($D = 2, V_{max} = 1, K_m = 0.5, C_{r_{max}} = 1, T_0 = 1, \alpha_1 = 0.5, \alpha_2 = 1, \alpha_3 = 0, \alpha_4 = 0, \alpha_5 = 0$). Full spatiotemporal dynamics can be found for (B) and (C) in supplementary animations.

2.2 Parameterisation

For the full multiscale model, describing the transport and metabolism of drugs in a multicellular *in-vitro* environment, it is useful to include quantitative, dimensional parameter values based on experimental data to directly represent the laboratory scenario for drugs with a range of physicochemical properties. Therefore, it is important to identify relevant parameter ranges for the microscale model before upscaling the problem to the multicellular/tissue level by introducing hepatic spheroid geometry. There are currently three key processes that determine drug dynamics in our system and require parameterisation: diffusion, metabolism and permeation. For simplicity and more general applicability, we will focus on the passive diffusion case and not cover carrier mediated transport during analysis of the multicellular model.

2.2.1 Diffusion of small molecule drugs

Most drugs, and nearly all drugs that cross the cell membrane via passive diffusion, are categorised as small molecule drugs. These are low molecular weight compounds and comprise most drugs on the market today (21). For a sample data base of 321 such drugs (22), we calculated diffusion coefficients based on physical measurements of weight and density (MW ~100-1,200Da; density ~0.6-2.6g/m³). Thus we propose the feasible diffusion coefficient range

of approximately 5×10^{-10} to $1 \times 10^{-9} \text{m}^2/\text{s}$ (further information in the supplementary material). This narrow range supports the assertion that the main determinants of drug disposition are the ability to translocate across hydrophobic diffusion barriers (permeability) and chemical transformation (metabolism), while variations in the aqueous diffusion rate have only minor effects on overall pharmacokinetics (13). A representative value of $7.5 \times 10^{-10} \text{m}^2/\text{s}$ for both D_I and D_E will be considered as default for further simulations.

2.2.2 Permeability as a function of lipophilicity

The permeability of a drug transported via passive diffusion is related to its lipophilicity, a measurable physicochemical property that can be used to define our permeability coefficient, Q. Menochet et al. (23, 24) discovered a log-linear relationship for hepatic uptake between passive diffusion clearance, P_{diff}, and lipophilicity,

$$\log P_{diff} = 0.6316 \times \text{LogD}_{7.4} - 0.3143 , \tag{10}$$

where P_{diff} has units of $\mu\text{L/min}/10^6\text{cells}$ and $\text{LogD}_{7.4}$ is a partition coefficient measure of lipophilicity at a physiologically relevant pH (pH = 7.4). This relationship allowed us to derive, Q, as a function of P_{diff}, and the radius of the cell, R, by taking into account passive uptake across the whole cell membrane of surface area $4\pi R^2$:

$$Q = \frac{P_{diff}}{4\pi R^2} = \frac{1}{10^6} \frac{10^{(0.6316 \times \text{LogD}_{7.4} - 0.3143)}}{4\pi R^2}. \tag{11}$$

For the full derivation see the supplementary material. $\text{LogD}_{7.4}$ values between 1 and 5 are considered within this study to represent relatively lipophilic, small-molecule drugs (relevant for passive diffusion), with $\text{LogD}_{7.4} = 3$ as default.

2.2.3   Simplified drug metabolism in hepatocytes

Metabolism represents the principal sink/removal term in our model and the metabolic rate is likely to vary greatly depending on the chemical makeup of the drug of study, as well as the quantity and activity of metabolising enzymes present. Therefore this term is likely to have a significant impact on the overall disposition of drug concentration in a metabolically active *in-vitro* spheroid system. Metabolic rates are assumed to be independent of space in the model for simplicity, although zonal variation may exist. Brown et al. (25) reported kinetic parameters for a range of compounds to predict metabolic clearance by using cryopreserved human hepatocytes. This publication provided pharmacologically feasible V_{max} (5×10^{-6} to 4.5×10^{-1} mol/m^3/s) and K_m (5×10^{-4} to 1.4×10^{-1}mol/m^3) ranges for drugs primarily metabolised in the liver and were thus used as conservative guidance for this model parameterisation, given that cells cultured in 3D often display improved drug metabolism functions. As default, we consider parameters values of $V_{max} = 5\times10^{-3}$mol/m^3/s and $K_m = 1\times10^{-2}$mol/m^3.

2.3   *Macroscale – hepatocyte spheroid geometry*

The impact of the hepatic spheroid environment on drug transport is considered by upscaling our microscale model to consider multiple discrete cells in a realistic spheroid geometry within an extracellular space (culture medium). This hepatocyte spheroid geometry was generated based upon histological staining of hepatic spheroids to provide representative cell sizes, number, and arrangement thereby replicating the *in-vitro* scenario within the multiscale mathematical model.

2.3.1 Mathematical description of spheroid geometry

Histological staining of a hepatocyte spheroid revealed the spatial distribution of the cell nuclei within a section (Figure 2A). This spatial information, as well as the spheroid boundary, was quantified digitally with WebPlotDigitizer (26) and imported into MATLAB. Due to the abundant expression of extracellular matrix in the hepatic spheroid histological images, it was not possible to visualise and/or quantify the location of the hepatocyte membranes. Therefore, we estimated the location of cell boundaries using Voronoi tessellation (Figure 2B). Briefly, Voronoi tessellation involves assigning regions to each nucleus such that any point in space within that region is closer to that nucleus than any other. The boundaries of these regions can be determined by drawing perpendicular bisectors between adjacent pairs of nuclei. This technique has been shown to provide viable estimates for the qualitative morphology of cells in a tissue (27).

Cellular ultrastructure was visualised by transmission electron microscopy (TEM). TEM revealed that the space between hepatocytes was narrow (~0.1-0.5μm, see Figure 2C). These values are supported by the literature which states intercellular spaces from 100nm to the μm-scale (28, 29). Furthermore, it should be noted that fixation methods can shrink such morphological features (30) and therefore we consider both narrow and wide intercellular space geometries. This was achieved by contracting the vertices of each model cell towards the cell's respective centre of mass by 1% ("narrow", ~0.2μm) or 10% ("wide", ~2μm) (Figure 2D).

2.3.2 Experimental methods

Primary rat hepatocyte spheroids with an initial seeding density of 5,000 cells were produced using the liquid-overlay technique as described by Kyffin et al. (31). After 11 days in culture

the spheroids were washed in PBS, fixed in 4% paraformaldehyde and subjected to routine histological processing before staining with haematoxylin or processed for TEM analysis. For TEM imaging, spheroids were fixed in 3% glutaraldehyde and processed as previously described (31). Ultrathin (~70–90nm) sections were examined using a FEI Tecnai Transmission Electron Microscope at an accelerating voltage of 80Kv and images taken using a Gatan digital camera.

2.3.3 Numerical simulation

The finite-element simulation software, COMSOL Multiphysics® 5.3, was used to solve the multiscale model PDEs. The 2D spheroid slice geometry was imported into COMSOL and the PDEs were defined as before to calculate the dynamics of drug concentration, C, for two separate phases (intracellular, C_I, and extracellular, C_E):

$$\frac{\partial C_I}{\partial t} = D_I \nabla^2 C_I - \frac{V_{max} C_I}{C_I + K_m}, \qquad\qquad C = C_I, \qquad (12)$$

$$\frac{\partial C_E}{\partial t} = D_E \nabla^2 C_E, \qquad\qquad C = C_E, \qquad (13)$$

with boundary conditions at every cell membrane within the spheroid,

$$(D_I \nabla C_I) \cdot \mathbf{n} = (D_E \nabla C_E) \cdot \mathbf{n} = Q(C_E - C_I), \qquad (14)$$

for the general inward fluxes, where **n** is the unit normal vector pointing out of each cell. An illustrative example of the multiscale model steady-state with a constant supply of drug at the outer boundary of the media phase ($C_{r_{max}}$ = 500µM) can be seen in Figure 2E, simulated for a drug with physicochemical properties based on the default parameter set described above. Note that permeability Q is related to LogD$_{7.4}$ according to equation (11). A 1D cross-section is

plotted in Figure 2F for visualisation, highlighting the discontinuities in drug concentration between intra- and inter-cellular space and the heterogeneity in drug concentration between cells in different regions.
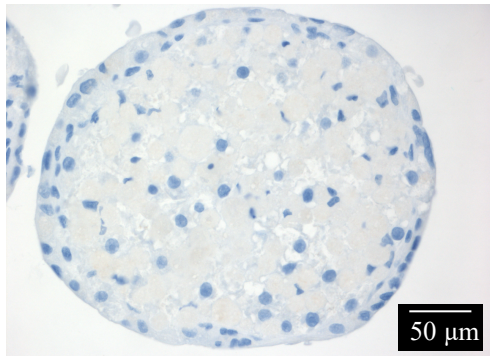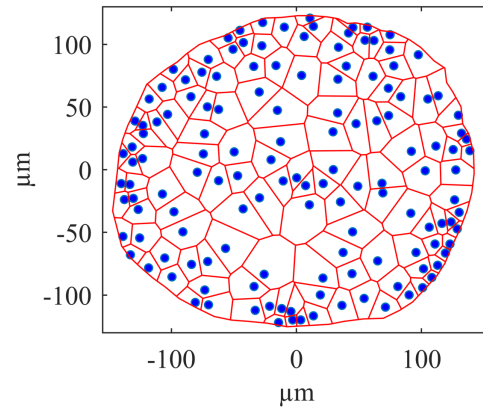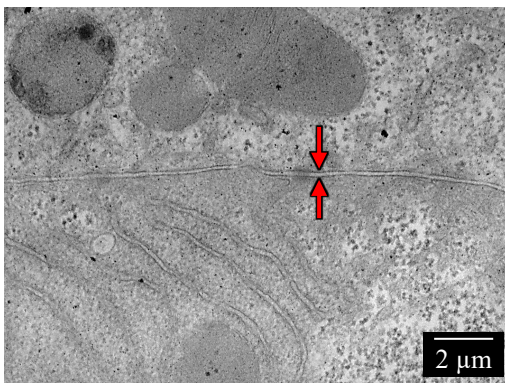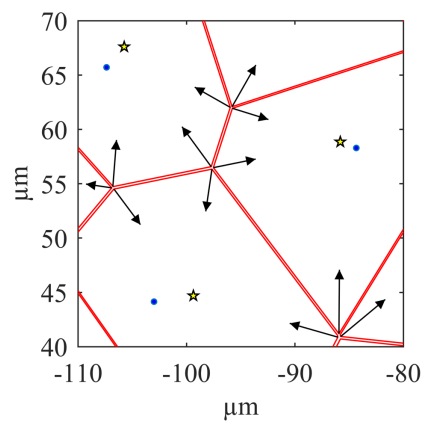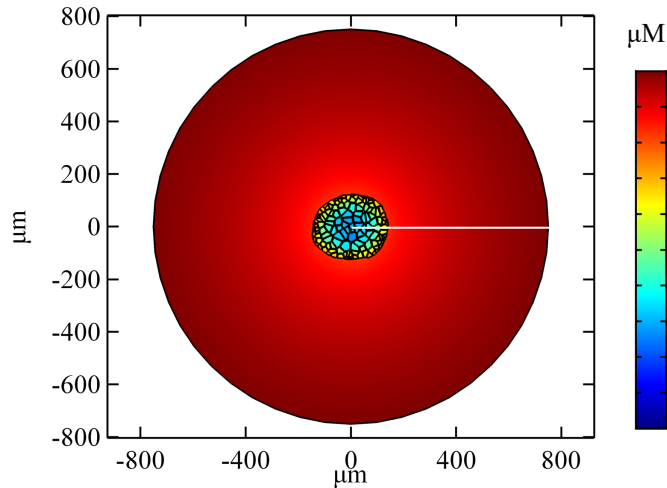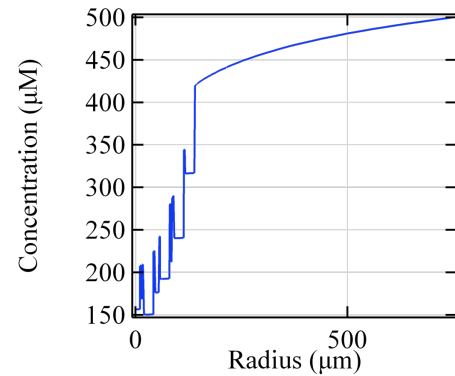
Figure 2: **The multiscale model including hepatocyte geometry.** (A): Histological staining of a hepatocyte spheroid slice indicating the location of cell nuclei (blue). (B): Voronoi diagram constructed to provide estimates of hepatocyte boundaries (red) based on location of hepatocyte nuclei (blue). (C): Representative TEM image of a hepatocyte spheroid showing the size of the space between adjacent cells. The intercellular space is indicated by the red arrows. (D): Intercellular space was introduced into

the model geometry by contracting the vertices of Voronoi cells (indicated by black arrows) towards the centre of each cell (yellow stars; nuclei in blue). (E): Steady-state distribution of an example drug ($LogD_{7.4}$ = 3 with default parameters and wide intercellular space), formed with a constant supply of 500µM at the outer media boundary (disc of radius 750µm). The drug distribution is denoted by the colour-bar, demonstrating that there are lower drug concentrations in the central hepatocytes. (F): A 1D cross-section of the simulation (position indicated by white line in (E)) signifies the variation of drug concentration inside and outside of the cells within the spheroid structure, as well as the heterogeneity of intracellular drug concentration in different regions of the spheroid.
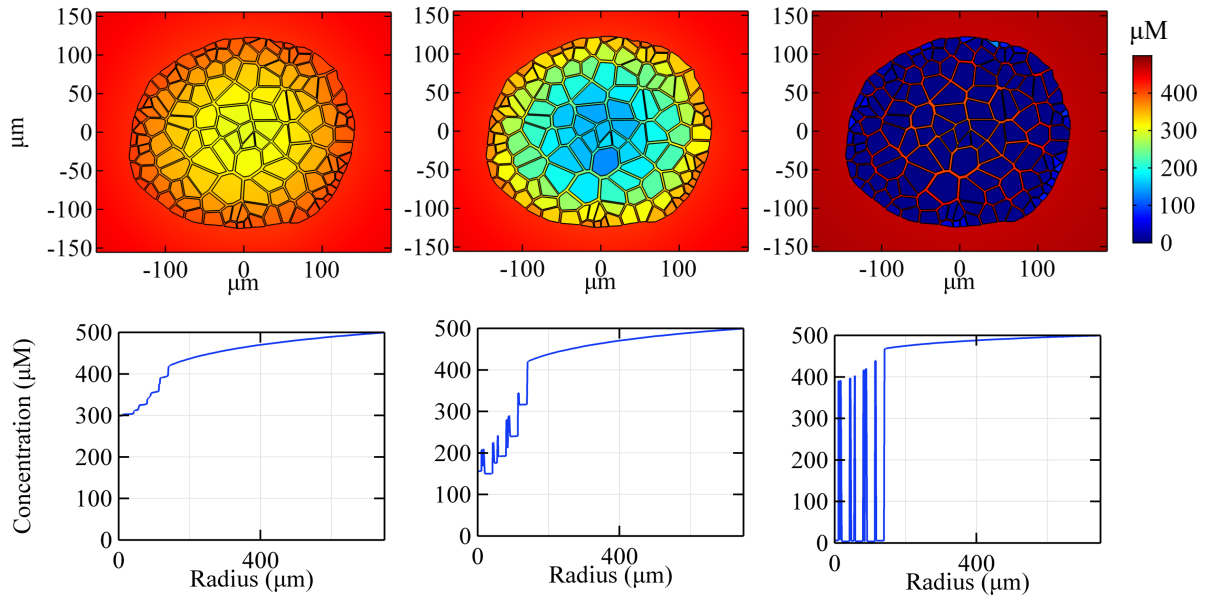
3   Results

3.1   *Impact of drug permeability on spatiotemporal distribution throughout spheroid*

The diffusion rate of a drug depends mainly on size, a property that has minimal variation in small molecule drugs (a detail supported by our analysis of over 300 compounds during parameterisation) and thus has relatively little impact upon drug distribution when compared with the ability to translocate across the hydrophobic diffusion barrier of the cell membrane (13). This translocation ability is determined by the lipophilicity of the drug during passive diffusional transfer across the membrane. Therefore we consider the impact that drug permeability (as determined by lipophilicity) has upon the overall dynamics within the representative *in-vitro* spheroid system. This analysis is illustrated by simulating the model, dosed for 3 example drugs with different permeability coefficients (corresponding to $LogD_{7.4}$ = 1, 3, 5, within the otherwise default parameter set) via constant supply at the external boundary and comparing the steady-state spatial distribution of drug concentration (Figure 3). Spatiotemporal dynamics can be found in supplementary animations.

The results indicate that for highly lipophilic drugs ($LogD_{7.4}$ = 5), the cell membrane does not represent a significant barrier to drug penetration and there is relatively little difference between drug concentrations in cells and the intercellular space. For relatively lowly lipophilic

drugs ($LogD_{7.4} = 1$), the membranes represent a significant barrier. Drug concentration is very low within the cells but relatively high in the intercellular space throughout the spheroid. However, in the intermediate case ($LogD_{7.4} = 3$), there is relatively little drug in the spheroid centre, both inside and outside of the hepatocytes. This is due to the balance between the overall processes of drug transport towards the spheroid centre (diffusion, permeability and metabolism), impacting penetration potential. Overall, it is clear that an increase in permeability results in higher intracellular drug concentration but there is a non-linear response in the intercellular space as permeability is increased, with a potential local minimum for drugs of intermediate lipophilicity. The same observations are made for narrow intercellular spaces and when varying transporter expression in the carrier-mediated transport model (data not shown). This result highlights the potential importance of not only permeability, but intercellular space on overall drug delivery.

Figure 3: **Impact of permeability on drug ~~dynamics~~ distribution.** Top row: Spatial distribution of drug concentration within a hepatic spheroid for 3 different permeability coefficients (permeability decrease from left to right, $LogD_{7.4} = 5, 3, 1$). The plots represent steady-state values after constant supply of 500µM at the outer media boundary (disc of radius 750µm). Bottom row: Corresponding representative 1D plots are provided for each drug using the same-cross section position as Figure 2E.

3.2   *Impact of intercellular dimensions on spatiotemporal distribution throughout spheroid*

Many mathematical models of cellular spheroids consider geometrical simplifications such as radial symmetry and a homogenous continuum of cells. The consideration of a spheroid with individual hepatocytes modelled as discrete regions in space, and accompanying intercellular space, has a visible impact upon the radial drug concentration profile. This can be seen most clearly in the case of low permeability with large fluctuations in the drug concentration between intra- and inter-cellular space (Figure 3). There is a considerable range of intercellular gap sizes within spheroids, a feature which can be magnified by fixation issues and cell type, with tumour spheroids notoriously exhibiting higher porosities (32). Therefore it is prudent to also consider

19

the impact of porosity (gap size) on drug delivery by simulating our model for both narrow and wide intercellular space geometries, as well as a model without intercellular space altogether for comparison. Steady-state spatial distributions in Figure 4 suggest that intercellular space has a considerable impact upon drug penetration, with increased porosity resulting in higher drug concentration for the spheroid interior.
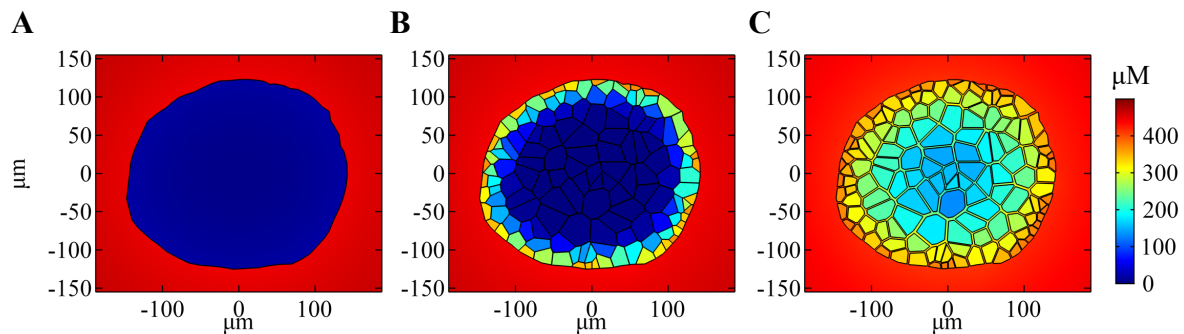

Figure 4: **Impact of intercellular space on drug ~~dynamics~~ distribution.** Spatial distribution of drug concentration within a hepatic spheroid for 3 different intercellular space geometries (no spaces (zero porosity, A); narrow spaces (~0.2µm, B); wide spaces (~2µm, C)). The figures represent steady-state values after constant supply of 500µM at the outer media boundary (disc of radius 750µm) with default parameters.

3.3 *Translating the multiscale model to a simple continuum model*

From Figure 4 it is clear that, when using quantitative, measurable, microscale parameters, the assumption of a homogenous continuum of hepatocytes in the spheroid will be insufficient for simulating spatial drug distributions, particularly for wider intercellular spaces. Therefore, we consider if there are any parameter modifications that can be made such that the continuum model can be said to sufficiently replicate the simulations provided by the more spatially complex discretised model. Such a model would be highly beneficial for the quantification of drug dynamics with greater computational efficiency. For this investigation we compare the average behaviour of the full discrete, multiscale, dimensional model ("cell-based model") with

20

the idealised radially symmetric, homogenised sphere model ("continuum model") in 2D (cylindrical coordinates) given by:

$$\frac{\partial C_S}{\partial t} = \frac{D_I^{Eff}}{r} \frac{\partial}{\partial r}\left(r\frac{\partial C_S}{\partial r}\right) - \frac{V_{max}C_S}{C_S + K_m}, \qquad r \leq R_S, \qquad (15)$$

$$\frac{\partial C_O}{\partial t} = \frac{D_E}{r} \frac{\partial}{\partial r}\left(r\frac{\partial C_O}{\partial r}\right), \qquad r > R_S, \qquad (16)$$

where C_S and C_O represent spheroid and outer drug concentrations respectively, and $R_S = 135$ μm (the average radius of the hepatocyte sphere slice in Figure 2), with boundary conditions

$$D_I^{Eff}\frac{\partial C_S}{\partial r} = 0, \qquad r = 0, \qquad (17)$$

$$D_I^{Eff}\frac{\partial C_S}{\partial r} = D_E\frac{\partial C_O}{\partial r} = Q^{Eff}(C_O - C_S), \qquad r = R_S, \qquad (18)$$

for effective parameters D_I^{Eff} and Q^{Eff} which represent the parameters to be modified. These parameters are logical targets for translation since they determine interior transport via internal diffusion and translocation across cell membranes in the cell-based model. Homogenisation here can be thought of as an extreme modification of the spheroid structure such that we reduce the system to a very large single cell with a single permeable membrane. The effective parameter values of the continuum model were optimised to fit the average behaviour of the cell-based models for both intercellular space geometries and a physicochemically relevant range of permeability coefficients (corresponding to $LogD_{7.4} = 1, 2, 3, 4, 5$). For information regarding parameter optimisation, see the supplementary material.

The required modifications of effective parameters, both collectively and individually as functions of drug lipophilicity and intercellular space, are summarised in Figure 5, as well as

corresponding error metrics. A combined parameter change metric in Figure 5E is introduced to quantify the relative amount of modification required for each scenario (intercellular width and lipophilicity) and defined as

$$\Delta P = \sqrt{\left(\frac{D_I^{Eff} - D_I}{D_I}\right)^2 + \left(\frac{Q^{Eff} - Q}{Q}\right)^2}. \tag{19}$$

From Figure 5 it is clear that ΔP is dominated by relative changes in the effective permeability coefficient, Q^{Eff} (compare Figure 5E with Figure 5A-B). Permeability must be increased to account for the intercellular space in the cell-based models (all lipophilicities), i.e., $Q^{Eff}/Q \geq$ 1 for all LogD$_{7.4}$ (Figure 5B). This effectively makes the spheroid boundary in the continuum model more porous (virtually simulating gaps between cells) and the discontinuity at the spheroid boundary is reduced. It should be noted that in the dimensional cell-based models, while D_I remains constant throughout all simulations, Q will change dependent on LogD$_{7.4}$ (recall equations (10)-(11)). This is seen in Figure 5C-D with absolute changes in Q^{Eff} and Q. Permeability must be increased by a greater amount for wider intercellular spaces to be effectively simulated by the continuum model (e.g., Figure 5D) for all LogD$_{7.4}$. This is expected due to the increased porosity provided by wider gaps. Finally, effective permeability must be increased by a greater amount for low lipophilicities. This can be seen in Figure 5B where the effective permeability Q^{Eff} decreases towards the dimensional value Q with increasing lipophilicity, for both gap sizes, in a monotonic fashion. This reflects the increased discrepancy between transport through cells and transport between cells found for drugs that are poorly lipid soluble.

In order for the continuum model to effectively simulate intercellular space, intracellular diffusion must be decreased for all lipophilicities, i.e., $D_I^{Eff} < D_I$ for all LogD$_{7.4}$ (Figure 5A). The primary effect of decreasing this parameter in the model is to increase the gradient of concentrations within the spheroid. For high lipophilicity and narrow intercellular spaces, the continuum model can provide a representative simulation of the cell-based model by reducing D_I^{Eff} alone. This property is observed by comparing the negligible changes in Q^{Eff} relative to D_I^{Eff} at high lipophilicity and narrow intercellular spaces. For example, when LogD$_{7.4}$ = 4 and 5, D_I is decreased by 94% and 86%, while Q is unchanged (Figure 5A-B). Theoretically, given a high enough value of LogD$_{7.4}$, this behaviour is expected for wide spaces too, but this is beyond relevant parameter space.

Regardless of lipophilicity, the optimised continuum model compares better with the cell-based model of narrow intercellular gaps (Figure 5F, solid lines). This is likely due to the relatively lower amount of fluctuations in the mean 1D profiles as there is less extracellular space in general within the spheroid. These fluctuations represent the local drug concentration variation at the cellular scale due to discrepancies between intra- and extra-cellular phases, which can be very high for drugs that are poorly lipid soluble (e.g., see Figure 3 1D profiles). Prior to any optimisation and re-scaling of dimensional parameters to their effective counterparts ($D_I \rightarrow D_I^{Eff}, Q \rightarrow Q^{Eff}$), there was a clear pattern in the fit quality between the simple continuum model approximation and the cell-based models of different sized intercellular spaces (Figure 5F, dashed lines). Generally, the continuum model fits the narrow spaces better for low membrane permeability and wider spaces better for high permeability. This feature appears to be correlated to the overall higher intracellular drug concentrations found in spheroids with

23

wider spaces (since there is proportionally less transport across metabolising cells). The (pre-optimised) continuum model exhibits very low drug concentration within the spheroid at low permeability and so fits the narrow-spaced model better. At higher permeabilities the continuum model has relatively high interior concentration and so fits the wide spaced cell-based model better (Figure S1 in the supplementary material). This switch in behaviour is likely due to the continuum model only providing a single barrier to permeation (spheroid boundary), which, once penetrated, facilitates drug penetration via diffusion solely.

Interestingly, Figure 5E indicates that the cell-based model with wider intercellular spaces requires more parameter modification for all drug lipophilicities. Despite the intra-spheroidal gradients being vastly different between the (pre-optimised) continuum and narrow cell-based model at high permeabilities (Figure S1), the boundary intracellular drug concentrations are similar. Therefore the continuum model can be optimised via sufficient reduction in D_I^{Eff} whilst maintaining the original permeability coefficient ($Q^{Eff} = Q$). However, in order to simulate the wide cell-based model, and account for different concentrations in boundary cells, a relatively greater change in Q^{Eff} was required (compare relative changes in effective parameters at LogD$_{7.4}$ = 4 and 5 for D_I^{Eff} and Q^{Eff} for both models, Figure 5A-B).
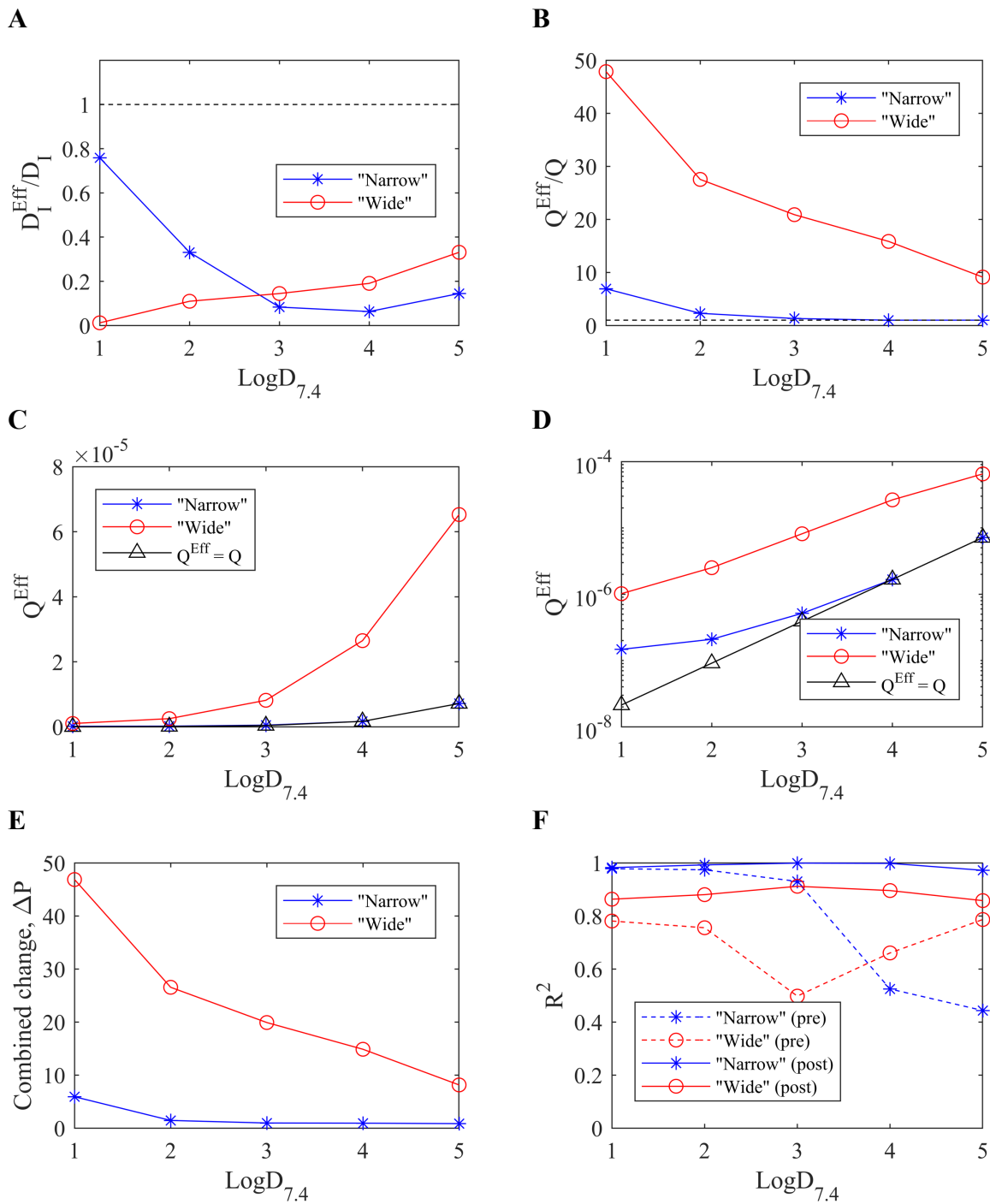
Figure 5: **Emulating the cell-based models with a simple, symmetric continuum model.** Effective parameters for intracellular diffusion and permeability (D_I^{Eff} and Q^{Eff}) were optimised in the continuum model to fit the output for the cell-based models for a range of drug lipophilicities. (A): The optimised D_I^{Eff} value provides the required relative changes in intracellular diffusion for the continuum model to match the cell-based models with narrow (blue) and wide (red) intercellular space geometries. (B) Required relative changes in permeability identified by optimising Q^{Eff}. Absolute values of Q^{Eff} optimised for each cell-based model and drug lipophilicity (LogD$_{7.4}$) are plotted in (C). (D): Optimised

Q^{Eff} on a log scale (y-axis). (E): A combined parameter change metric (ΔP) indicates the summarised amount of model modification required for the continuum model to effectively simulate the cell-based models. (F): Comparisons between model outputs are calculated by using the R^2 error metric to determine relative quality of fits (see supplementary material for definition). Comparisons are made both prior to optimisation ("pre", direct comparison using dimensional parameters, i.e., $D_I^{Eff} = D_I, Q^{Eff} = Q$) and post-optimisation ("post").

3.4 *Investigating the impact of permeability on the dynamic process of drug delivery in different regions of the spheroid for a bolus dose*

Intercellular space has a discernible impact on the spatiotemporal drug dynamics in the *in-vitro* spheroid environment and moreover, a non-linear effect was revealed for local concentrations within intercellular space as permeability is increased (Figure 3). Since this phenomenon (i.e., a monotonic decrease in intracellular drug concentration with decreasing permeability, but a non-monotonic response in the intercellular regions) cannot be described by the simple continuum model, it is worth considering the potential impact of this feature on drug penetration. Here we choose to examine drug delivery and subsequent effects by calculating the total uptake/metabolism of the drug in different regions of the spheroid. To investigate drug delivery via metabolism, we introduce the following "metabolism" variable, M, with dynamics:

$$\frac{\partial M}{\partial t} = \frac{V_{max}C}{C + K_m}, \qquad\qquad C = C_I, \qquad (20)$$

which corresponds to accumulated drug metabolised and is only relevant inside model cells. Corresponding model simulations are conducted with a finite bolus dose initially supplied in the outer medium, uniformly distributed in the extracellular space outside the spheroid, and zero-flux boundary conditions are imposed on the outer boundary of the media phase.

Two separate regions are defined, "outer" and "inner", corresponding to cells of comparable size in the outer boundary layer of the spheroid, (x, y) = (-10μm, 110μm), and the spheroid centre, (x, y) = (0μm, 0μm). Simulations are run to the drug-free steady-state whereby all of the initial dose has been removed from the system and accumulated in the effective sink variable, M. For highly lipophilic drugs, the concentration dynamics are relatively similar between inner and outer regions as the drug is able to be transported throughout the spheroid quickly, unrestricted by permeability. However, the outer cells are exposed to slightly higher concentrations and consequently more drug is metabolised in this region, demonstrated by similar rates of metabolism (Figure 6A). Simulations of lowly lipophilic drugs require much longer timespans in order to reach equilibrium due to the reduced uptake rate at the cell membranes. However, due to the intercellular transport via diffusion, even centrally located cells receive relatively high local drug exposure and metabolise at a similar rate to outer cells (Figure 6C). It is the *in-silico* drugs of intermediate lipophilicity in this model scenario that exhibit the most striking discrepancies between inner and outer cells (Figure 6B). The impact of these varying rates of metabolism between drug lipophilicities and regions of the spheroid can be evaluated by comparing the total drug metabolised (Figure 6D). The greatest discrepancy in drug uptake between outer and inner hepatocytes is revealed for drugs of intermediate permeability (1,250% increase from inner to outer cells for $LogD_{7.4} = 4$ compared to just +13% for $LogD_{7.4} = 1$ and +219% for $LogD_{7.4} = 6$). Furthermore, outer cells in this case receive the most drug out of all three cases studies and the inner cells receive the least (Figure 6D). This effect can potentially be exacerbated when carrier-mediated transport kinetics are modelled at the cell membrane, due to the saturating effects of this uptake mechanism (arbitrary

transporter parameterisation, data not shown). This feature has the potential to significantly impact experimental design considerations and *in-vitro* drug efficacy and toxicity evaluation.
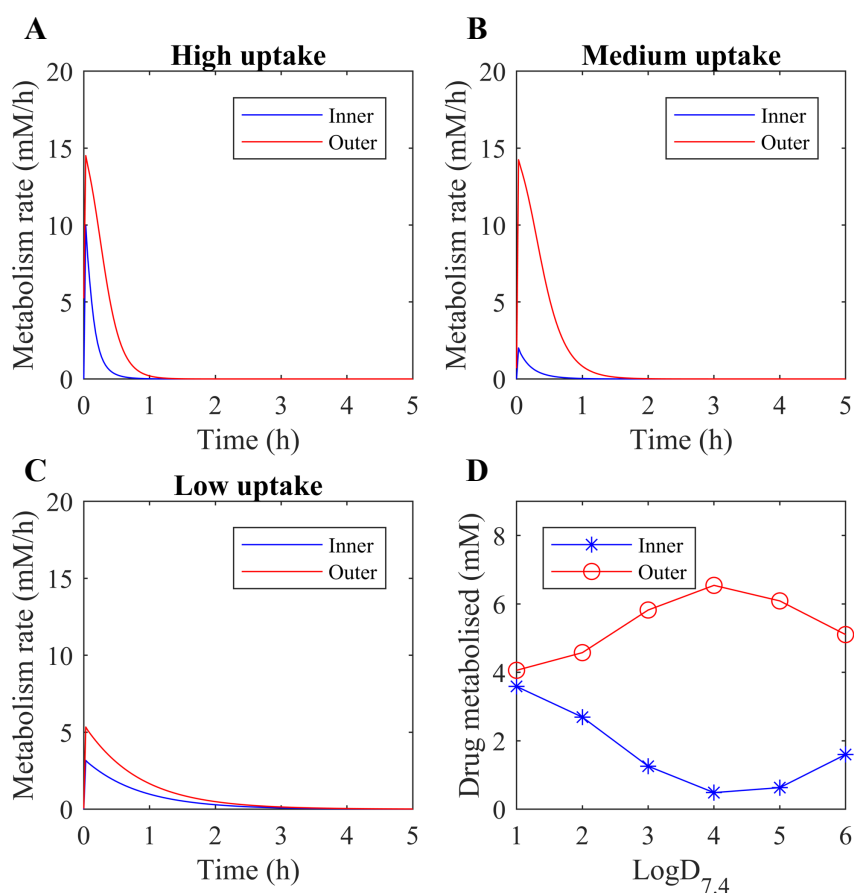

Figure 6: **Impact of drug lipophilicity on uptake and metabolism in different regions of the spheroid.** Metabolism rates are plotted against time as a result of model simulations following a bolus dose of 100μM, initially uniformly distributed in the medium for varying drug lipophilicities ($LogD_{7.4}$ = 6 (A), 4 (B), 2 (C)). (D): Total metabolised drug (after complete clearance) is compared for inner and outer hepatocytes within the spheroid for a range of drug lipophilicities ($LogD_{7.4}$ = 1-6).

4 Discussion

The enhanced sophistication of current cell culture methodologies due to increasing advancements in scientific understanding and technological developments has allowed for *in-vitro* studies to become more physiologically relevant. There are a range of different *in-vitro* models that span varying levels of complexity, reproducibility, high-throughput potential, and

cost. Spheroids represent an intermediate experimental model that allows for increased physiological relevance over 2D monolayers due to the 3D environment, as well as more appropriate cell morphology and functionality while remaining cost-effective, consistent, and easy to use (1). The subsequent prevalence of liver spheroid cultures for studying hepatocyte behaviour *in-vitro* is evident and represents a key component of drug development such that drug candidates can be tested for efficacy and toxic potential in a 3D environment with physiological gradients (31, 33-35). Data-driven multiscale mathematical models provide an ideal platform from which to try and enhance mechanistic understanding of new biotechnologies by simulating the underlying physical processes. Additionally, the development of spatiotemporal data generated by 3D cell imaging offers tremendous opportunities for developing, parameterising and testing multiscale mathematical models and in response, mathematical modelling can be successfully used to optimise these developing technologies.

In this study we developed a mathematical model of drug transport and metabolism in a multiscale spheroid framework, accounting for microscale processes such as membrane transport kinetics and how they relate to the physicochemical properties of a drug, and macroscale features such as the geometry of a hepatocyte spheroid, informed by imaging data. Cellular uptake of drugs was modelled by the two major processes of transport across the cell membrane, passive diffusion and carrier-mediated transport (17). The carrier-mediated transport microscale model was innately more complex, depending on quantities such as transporter protein expression, binding kinetics and rates of conformational change and this complexity allowed for a wider array of dynamic mechanisms such as enzymatic saturation and active processes. The extensive parameterisation required to quantify the carrier-mediated

transport model depends on more compound-specific information, and so the passive diffusion case became the main focus of investigations within the generalised multiscale framework, more relevant for relatively lipophilic compounds.

The explicit representation of individual hepatocytes based on imaging data allowed for an investigation into the effects of including a distinct cell-based geometry in the model. The model suggests that steady-state intracellular drug concentrations increase monotonically with increasing drug lipophilicity. However, a non-monotonic relationship was revealed between drug lipophilicity and intercellular drug concentration (Figure 3), while the width of the intercellular space further impacted spatial drug distribution (Figure 4). Intercellular space geometry, or spheroid porosity, is therefore a key physiological feature of the multicellular structure but is both difficult to accurately quantify and known to vary widely between cell types. This is particularly relevant in the case of tumour-derived spheroids, whose morphology tends to be more porous (32), and organoids that are increasingly being used in efficacy testing for tumour cells (36). We therefore studied two different average intercellular widths informed by TEM data and the literature which suggested a range of 10^2-10^3nm-scale, with results varying due to cell type, tumour phenotype and experimental artefacts such as fixation (29, 30, 37).

While it is important to account for intercellular space within spheroids to correctly model drug delivery, the consequent increase in complexity by modelling this feature explicitly renders detailed analytic work intractable and deriving numerical solutions is costly with respect to time and computational power requirements. Therefore it is appropriate to consider the application of simplified models that consider averaged or homogenised system behaviour and under what conditions they can provide valid approximations (38). We have shown how to

approximate the cell-based models using a simple, symmetric, continuum model by reparameterising dimensional parameters to re-scaled effective counterparts. For relatively narrow intercellular gaps, these approximations are more accurate and the required parameter changes are reduced. The differences between the models, due to the explicit representation of intercellular space (porosity) within the cell-based model, are largely accounted for by increasing the effective permeability parameter. This increase in the effective permeability increases the drug transport across the spheroid boundary in the continuum model. This is particularly important at lower lipophilicities when permeability limitations are maximised. For higher lipophilicities and narrow intercellular space, the spatially averaged dynamics of the cell-based model can be effectively simulated with the symmetric continuum model by appropriate reductions in the effective internal diffusion parameter only. Further work is required to determine the impact of spatially varying quantities that might exist within a spheroid such as intercellular space or transporters that vary zonally (39), and how these might compare between continuum models and cell-based models. Metabolic rates are also known to vary in space throughout multicellular structures due to gradients in environmental factors such as oxygen and glucose (40). Alternative model simplifications that might expedite analysis can be made by careful consideration of potentially redundant model complexities such as intracellular diffusion, which may be neglected in some scenarios. The model currently neglects any intracellular binding of the drug for simplicity, focusing on the dominant mechanisms of transport and removal (metabolism) that drive the spatiotemporal dynamics. However, for specific future applications of the model, intracellular binding could be considered by ascertaining the relevant fraction unbound for a particular drug, as this will lower

31

the rate of metabolism for those drugs which bind strongly to intracellular proteins and nuclear structures.

The discovery of an apparent local minimum in drug penetration, whereby intercellular concentrations are lower for intermediate membrane permeation, motivated an investigation into corresponding effects on drug delivery, uptake and metabolism in spheroid centres for a bolus dose (Figure 6). The results of this investigation indicated that indeed, it is feasible to observe minimal drug uptake at the spheroid centre for drugs of intermediate lipophilic properties (with the majority of drug being metabolised at the outer regions). These mechanistic insights and modelling results have potential impact for the dosing of spheroid systems *in-vitro* as well as relevance for analogous *in-vivo* systems such as avascular tumours. It is not necessarily sufficient to assume that increasing a chemical's lipid solubility will enhance its metabolism at the spheroid centre. Lowly lipid soluble drugs may require a much longer time in culture but ultimately metabolise the drug more uniformly throughout the spheroid. Accounting for reduced penetration due to the intermediate lipophilic property may be alleviated somewhat by increasing the dose, but this could have potentially toxic consequences from overdosing cells at the spheroid boundary. Other experimental design options include manipulating permeability (by chemical modification or intervention, but this could potentially further increase the divergent amounts of drug being metabolised in different regions of the spheroid) or using smaller spheroids. These investigations could be conducted within the *in-silico* framework, in the first instance, to guide strategy. The implications of drug delivery characteristics based on permeability parameters could potentially be translated to targeting delivery in tissues of multiple cell types expressed zonally. For example, targeting the central zone of a spheroid that contains cells of a different phenotype (e.g. cancerous/hypoxic) may be

aided by manipulating these properties regarding permeability, i.e., making certain that the permeability is either relatively high or relatively low to ensure delivery to the spheroid centre. Validation of these *in silico* investigations could involve emerging technologies such as MALDI (matrix-assisted laser desorption/ionization)-Mass Spectrometry Imaging, which provide label-free mass spectrometric detection within tissue sections (41). This detection methodology is rapidly being developed to provide a quantitative measure of drug penetration within a tissue/spheroid at different time-points that could potentially be compared with our model. The combination of mathematical modelling with experimental imaging provides a convenient *in-silico* testing toolkit to optimise the use of 3D cell culture systems in the laboratory and maximise the potential of spheroid models aiding drug discovery, toxicity testing and dose optimisation.

Author Contributions

JAL wrote the manuscript; JAK, ALH, HEC, CM, & PS performed the experiments; JAL, SDW & RNB contributed to the mathematical modelling; JAL, DPW, SDW & RNB designed the research. All authors read and approved the final manuscript.

Declaration of Interests

The authors declare no competing interests.

References

1.   Kyffin JA, Sharma P, Leedale J, Colley HE, Murdoch C, Mistry P, et al. Impact of cell types and culture methods on the functionality of in vitro liver systems-A review of cell systems for hepatotoxicity assessment. Toxicology In Vitro. 2018;48:262-75.

2.   Hoarau-Véchot J, Rafii A, Touboul C, Pasquier J. Halfway between 2D and animal models: are 3D cultures the ideal tool to study cancer-microenvironment interactions? International journal of molecular sciences. 2018;19(1):181.

3.   Fang Y, Eglen RM. Three-dimensional cell cultures in drug discovery and development. SLAS DISCOVERY: Advancing Life Sciences R&D. 2017;22(5):456-72.

4.   Bell CC, Dankers AC, Lauschke VM, Sison-Young R, Jenkins R, Rowe C, et al. Comparison of hepatic 2D sandwich cultures and 3D spheroids for long-term toxicity applications: a multicenter study. Toxicological Sciences. 2018;162(2):655-66.

5.   Williams DP, Shipley R, Ellis MJ, Webb S, Ward J, Gardner I, et al. Novel in vitro and mathematical models for the prediction of chemical toxicity. Toxicology research. 2013;2(1):40-59.

6.   Karolak A, Markov DA, McCawley LJ, Rejniak KA. Towards personalized computational oncology: from spatial models of tumour spheroids, to organoids, to tissues. J R Soc Interface. 2018;15(138):20170703.

7.   Visser S, Alwis D, Kerbusch T, Stone J, Allerheiligen S. Implementation of quantitative and systems pharmacology in large pharma. CPT: pharmacometrics & systems pharmacology. 2014;3(10):1-10.

8.   Sturla SJ, Boobis AR, FitzGerald RE, Hoeng J, Kavlock RJ, Schirmer K, et al. Systems toxicology: from basic research to risk assessment. Chemical research in toxicology. 2014;27(3):314-29.

9.   Turner RM, Park BK, Pirmohamed M. Parsing interindividual drug variability: an emerging role for systems pharmacology. Wiley Interdisciplinary Reviews: Systems Biology and Medicine. 2015;7(4):221-41.

10.   Krewski D, Acosta Jr D, Andersen M, Anderson H, Bailar III JC, Boekelheide K, et al. Toxicity testing in the 21st century: a vision and a strategy. Journal of Toxicology and Environmental Health, Part B. 2010;13(2-4):51-138.

11.   Raies AB, Bajic VB. In silico toxicology: computational methods for the prediction of chemical toxicity. Wiley Interdisciplinary Reviews: Computational Molecular Science. 2016;6(2):147-72.

12.   Pridgeon CS, Schlott C, Wong MW, Heringa MB, Heckel T, Leedale J, et al. Innovative organotypic in vitro models for safety assessment: aligning with regulatory requirements and understanding models of the heart, skin, and liver as paradigms. Archives of toxicology. 2018;92(2):557-69.

13.   Rang H, Dale M, Ritter J, Moore P. Pharmacology, 5th edn: Churchill Livingston; 2003.

14.	Dobson PD, Kell DB. Carrier-mediated cellular uptake of pharmaceutical drugs: an exception or the rule? Nature Reviews Drug Discovery. 2008;7(3):205-20.

15.	Kell DB. What would be the observable consequences if phospholipid bilayer diffusion of drugs into cells is negligible? Trends in pharmacological sciences. 2015;36(1):15-21.

16.	Sugano K, Kansy M, Artursson P, Avdeef A, Bendels S, Di L, et al. Coexistence of passive and carrier-mediated processes in drug transport. Nature reviews Drug discovery. 2010;9(8):597-614.

17.	Cocucci E, Kim JY, Bai Y, Pabla N. Role of Passive diffusion, Transporters, and membrane trafficking-mediated processes in cellular drug transport. Clinical Pharmacology & Therapeutics. 2017.

18.	Nigam SK. What do drug transporters really do? Nature reviews Drug discovery. 2015;14(1):29.

19.	Keener JP, Sneyd J. Mathematical physiology: Springer; 1998.

20.	Wood BD, Whitaker S. Diffusion and reaction in biofilms. Chemical Engineering Science. 1998;53(3):397-425.

21.	AstraZeneca.	Small	Molecules	2019	[Available	from: https://www.astrazeneca.com/what-science-can-do/drug-modalities/small-molecule.html.

22.	Kyffin JA. Establishing species-specific 3D liver microtissues for repeat dose toxicology and advancing in vitro to in vivo translation through computational modelling [PhD Thesis]: Liverpool John Moores University; 2018.

23.	Ménochet K, Kenworthy KE, Houston JB, Galetin A. Use of mechanistic modeling to assess interindividual variability and interspecies differences in active uptake in human and rat hepatocytes. Drug Metabolism and Disposition. 2012;40(9):1744-56.

24.	Ménochet K, Kenworthy KE, Houston JB, Galetin A. Simultaneous assessment of uptake and metabolism in rat hepatocytes: a comprehensive mechanistic model. Journal of Pharmacology and Experimental Therapeutics. 2012;341(1):2-15.

25.	Brown HS, Griffin M, Houston JB. Evaluation of cryopreserved human hepatocytes as an alternative in vitro system to microsomes for the prediction of metabolic clearance. Drug metabolism and disposition. 2007;35(2):293-301.

26.	Rohatgi A. WebPlotDigitizer Austin, Texas, USA2018 [4.1:[Available from: https://automeris.io/WebPlotDigitizer.

27.	Kaliman S, Jayachandran C, Rehfeldt F, Smith A-S. Limits of Applicability of the Voronoi Tessellation Determined by Centers of Cell Nuclei to Epithelium Morphology. Frontiers in physiology. 2016;7:551.

28.	Goodman TT, Chen J, Matveev K, Pun SH. Spatio-temporal modeling of nanoparticle delivery to multicellular tumor spheroids. Biotechnology and bioengineering. 2008;101(2):388-99.

29.   Gao Y, Li M, Chen B, Shen Z, Guo P, Wientjes MG, et al. Predictive models of diffusive nanoparticle transport in 3-dimensional tumor cell spheroids. The AAPS journal. 2013;15(3):816-31.

30.   Chatterjee S. Artefacts in histopathology. Journal of oral and maxillofacial pathology: JOMFP. 2014;18(Suppl 1):S111.

31.   Kyffin JA, Sharma P, Leedale J, Colley HE, Murdoch C, Harding AL, et al. Characterisation of a functional rat hepatocyte spheroid model. Toxicology in Vitro. 2019;55:160-72.

32.   Li Y, Wang J, Wientjes MG, Au JL-S. Delivery of nanomedicines to extracellular and intracellular compartments of a solid tumor. Advanced drug delivery reviews. 2012;64(1):29-39.

33.   Andersson TB. Evolution of novel 3D culture systems for studies of human liver function and assessments of the hepatotoxicity of drugs and drug candidates. Basic & clinical pharmacology & toxicology. 2017;121(4):234-8.

34.   Hendriks DF, Puigvert LF, Messner S, Mortiz W, Ingelman-Sundberg M. Hepatic 3D spheroid models for the detection and study of compounds with cholestatic liability. Scientific reports. 2016;6:35434.

35.   Bell CC, Hendriks DF, Moro SM, Ellis E, Walsh J, Renblom A, et al. Characterization of primary human hepatocyte spheroids as a model system for drug-induced liver injury, liver function and disease. Scientific reports. 2016;6:25187.

36.   Kopper O, de Witte CJ, Lõhmussaar K, Valle-Inclan JE, Hami N, Kester L, et al. An organoid platform for ovarian cancer captures intra-and interpatient heterogeneity. Nature Medicine. 2019:1.

37.   Leroux C-E, Monnier S, Wang I, Cappello G, Delon A. Fluorescent correlation spectroscopy measurements with adaptive optics in the intercellular space of spheroids. Biomedical optics express. 2014;5(10):3730-8.

38.   Wood BD, Quintard M, Whitaker S. Calculation of effective diffusivities for biofilms and tissues. Biotechnology and bioengineering. 2002;77(5):495-516.

39.   Tomlinson L, Hyndman L, Firman JW, Bentley R, Kyffin JA, Webb SD, et al. In vitro liver zonation of primary rat hepatocytes. Frontiers in bioengineering and biotechnology. 2019;7.

40.   Sheth DB, Gratzl M. Electrochemical mapping of oxygenation in the three-dimensional multicellular tumour hemi-spheroid. Proceedings of the Royal Society A. 2019;475(2225):20180647.

41.   Winter M, Bretschneider T, Kleiner C, Ries R, Hehn J P, Redemann N, Luippold A H, Bischoff D and Büttner F H (2018) Establishing MALDI-TOF as versatile drug discovery readout to dissect the PTP1B enzymatic reaction. *SLAS DISCOVERY: Advancing Life Sciences R&D* 23: 561-573.

SUPPLEMENTARY MATERIAL:

Multiscale modelling of drug transport and metabolism in liver spheroids

Joseph A. Leedale[1], Jonathan A. Kyffin[2], Amy L. Harding[3], Helen E. Colley[3], Craig Murdoch[3], Parveen Sharma[4], Dominic P. Williams[5], Steven D. Webb[1,2], Rachel N. Bearon[1]

[1]EPSRC Liverpool Centre for Mathematics in Healthcare, Dept. of Mathematical Sciences, University of Liverpool, Liverpool, L69 7ZL, UK

[2]Dept. of Applied Mathematics, Liverpool John Moores University, Liverpool, L3 3AF, UK

[3]School of Clinical Dentistry, University of Sheffield, Claremont Crescent, Sheffield, S10 2TA, UK

[4]MRC Centre for Drug Safety Science, Dept. of Molecular and Clinical Pharmacology, University of Liverpool, Liverpool, L69 3GE, UK

[5]AstraZeneca, IMED Biotech Unit, Drug safety & Metabolism, Cambridge Science Park, Cambridge, CB4 0FZ, UK

Contents

1   Microscale Transport

The mathematical representation of microscale drug transport across a cell membrane can be studied with a simple model that considers the processes governing drug concentration dynamics in two phases, inside and outside the cell, with a permeable barrier in-between. Assume diffusion occurs at different rates inside (D_I) and outside (D_E) of a spherical cell of radius R and that the drug is metabolised within the cell. The drug concentration (C) dynamics inside the cell are given by the partial differential equation (PDE):

$$\frac{\partial C}{\partial \tilde{t}} = \tilde{\nabla}^2 C - \frac{\tilde{V}_{max} C}{C + K_m} , \tag{S1}$$

with scaling

$$\tilde{x} = \frac{x}{R} , \qquad \tilde{t} = \frac{D_I}{R^2} t , \qquad \tilde{V}_{max} = \frac{R^2}{D_I} V_{max} , \tag{S2}$$

where V_{max} is the maximum metabolism rate and K_m represents the drug concentration at which metabolism is half maximal. Note that the metabolism of the drug is assumed to occur with Michaelis-Menten kinetics, which is relevant for enzyme-mediated biochemical reactions but here prohibits the derivation of an analytical solution at the steady state. Assume that outside the cell drug transport is governed by diffusion processes only:

$$\frac{\partial C}{\partial \tilde{t}} = D \tilde{\nabla}^2 C , \tag{S3}$$

where $D = D_E/D_I$. For simplicity, assume that the problem is radially symmetric, drop the tildes and convert to spherical coordinates for a 1D representative model with respect to the radius, r.

$$\frac{\partial C}{\partial t} = \frac{1}{r^2} \frac{\partial}{\partial r} \left(r^2 \frac{\partial C}{\partial r} \right) - \frac{V_{max} C}{C + K_m} , \qquad\qquad r \le 1 , \tag{S4}$$

$$\frac{\partial C}{\partial t} = \frac{D}{r^2} \frac{\partial}{\partial r} \left(r^2 \frac{\partial C}{\partial r} \right) , \qquad\qquad r > 1 . \tag{S5}$$

We impose the following boundary conditions for the cell centre ($r = 0$) and a distance away from the cell $r = r_{max}$:

$$\frac{\partial C}{\partial r} = 0 , \qquad\qquad r = 0 , \tag{S6}$$

$$C = C_{r_{max}} , \qquad\qquad r = r_{max} , \tag{S7}$$

where $C_{r_{max}}$ is a constant supply term to be prescribed. Assume that the flux at the sphere boundary is equal such that mass is conserved, i.e.,

$$D_I \frac{\partial C_I}{\partial r} = D_E \frac{\partial C_E}{\partial r}, \qquad\qquad r = 1, \qquad\qquad \text{(S8)}$$

where C_I and C_E are used to distinguish between interior and exterior drug concentrations at the cell membrane boundary. A further boundary condition must be specified at the cell membrane boundary in order to solve the coupled PDE system and investigate the effects of different means of drug transport.

1.1 Passive diffusion

To determine the boundary condition describing the flux of drug into the cell due to passive diffusion, consider an additional compartment, i.e., the cell membrane. It is assumed that within this compartment, drug transport is determined solely by aqueous diffusion. Since the thickness of the membrane (~5-10 nm) is much smaller than the cell radius (~10-20 μm) and surrounding cell space, it is assumed that the drug diffuses across the space between the lipid barriers of the membrane relatively quickly compared to transport outside. Therefore, we assume that there is a valid quasi-steady state assumption to be made at either side of the membrane such that drug concentration can be assumed to be constant at the lipid barriers on this quick timescale. Mathematically, we can represent this as a thin membrane compartment of width ϵ in which the drug concentration (C_M) is transported across the space via diffusion (at a rate D_M) with Dirichlet boundary conditions:

$$\frac{\partial C_M}{\partial t} = \frac{D_M}{r^2} \frac{\partial}{\partial r}\left(r^2 \frac{\partial C_M}{\partial r}\right) \approx 0, \qquad\qquad \text{(S9)}$$

$$C_M = C_I = \text{constant}, \qquad\qquad r = 1, \qquad\qquad \text{(S10)}$$

$$C_M = C_E = \text{constant}, \qquad\qquad r = 1 + \epsilon. \qquad\qquad \text{(S11)}$$

We can solve equation (S9) via integration to give

$$C_M = -\frac{A}{r} + B, \qquad\qquad \text{(S12)}$$

where A and B are constants that are determined using the boundary conditions (S10)-(S11) such that

$$A = -\frac{1+\epsilon}{\epsilon}(C_E - C_I), \qquad B = C_I - \frac{1+\epsilon}{\epsilon}(C_E - C_I), \qquad\qquad \text{(S13)}$$

Therefore, by substitution into (S12), we acquire the solution

$$C_M = C_I + \frac{1+\epsilon}{\epsilon}\left(\frac{1}{r} - 1\right)(C_E - C_I) \qquad\qquad \text{(S14)}$$

$$\approx C_I + \frac{1}{\epsilon}\left(\frac{1-r}{r}\right)(C_E - C_I), \qquad\qquad \text{(S15)}$$

for $\epsilon \ll 1$. The inward flux at the cell membrane can then be found by Fick's law:

4

$$J = -D_M \frac{\partial C_M}{\partial r} = -D_M \frac{1}{\epsilon r^2}(C_E - C_I) = \frac{D_M}{\epsilon}(C_I - C_E). \qquad r = 1. \qquad \text{(S16)}$$

where $D_M/\epsilon = Q$ represents the permeability coefficient, proportional to the rate of intra-membrane aqueous diffusion and inversely proportional to the thickness of the membrane. Since $\epsilon \ll 1$ we can show that the outer membrane flux can also be derived such that

$$J = -D_M \frac{\partial C_M}{\partial r} = -D_M \frac{1}{\epsilon + 2\epsilon^2 + \epsilon^3}(C_E - C_I) \approx \frac{D_M}{\epsilon}(C_I - C_E). \qquad r = 1 + \epsilon, \qquad \text{(S17)}$$

and the inner and outer fluxes are equal as $\epsilon \to 0$ and thus,

$$D_I \frac{\partial C_I}{\partial r} = Q(C_E - C_I) = D_E \frac{\partial C_E}{\partial r}, \qquad r = 1. \qquad \text{(S18)}$$

1.1.1   Numerical solution

We can solve the system numerically using the method of lines and gears whereby the following finite difference approximations in the spatial dimension reduce our PDE problem to an ODE problem. We apply central difference formulae for 1st and 2nd order spatial derivatives:

$$\frac{\partial C(r,t)}{\partial r} = \frac{C(r + \Delta r, t) - C(r - \Delta r, t)}{2\Delta r}, \qquad \text{(S19)}$$

$$\frac{\partial^2 C(r,t)}{\partial r^2} = \frac{C(r + \Delta r, t) - 2C(r,t) + C(r - \Delta r, t)}{(\Delta r)^2}. \qquad \text{(S20)}$$

Therefore, we can re-write our PDE model for interior dynamics in equation (S4) as

$$\frac{\partial C}{\partial t} = \frac{1}{r^2}\frac{\partial}{\partial r}\left(r^2 \frac{\partial C}{\partial r}\right) - \frac{V_{max}C}{C + K_m} = \frac{\partial^2 C}{\partial r^2} + \frac{2}{r}\frac{\partial C}{\partial r} - \frac{V_{max}C}{C + K_m}, \qquad \text{(S21)}$$

$$\Rightarrow \frac{dC_i}{dt} = \frac{1}{\Delta r}\left(\frac{C_{i+1} - 2C_i + C_{i-1}}{\Delta r} + \frac{C_{i+1} - C_{i-1}}{r}\right) - \frac{V_{max}C_i}{C_i + K_m}, \qquad \text{(S22)}$$

for $i = 1..R$ ($r = 0..1$) where we use notation $C_{i+1} = C(r + \Delta r, t)$ such that an increase by 1 in subscript i corresponds to a radial increment in Δr as defined by the discretisation of the mesh (spatial domain). Similarly our PDE model for exterior dynamics is reduced to

$$\frac{dC_i}{dt} = \frac{D}{\Delta r}\left(\frac{C_{i+1} - 2C + C_{i-1}}{\Delta r} + \frac{C_{i+1} - C_{i-1}}{r}\right), \qquad \text{(S23)}$$

for $i = R + 1..N + 1$ ($r = 1 + \Delta r..r_{max}$). We now inspect our boundary conditions in order to determine special case boundary values.

1.1.1.1   Sphere centre boundary

In the case where $i = 1$ we have

$$\frac{dC_1}{dt} = \frac{1}{\Delta r}\left(\frac{C_2 - 2C_1 + C_0}{\Delta r} + \frac{C_2 - C_0}{r}\right) - \frac{V_{max}C_1}{C_1 + K_m}, \tag{S24}$$

and therefore a singularity at $r = 0$. In the limit,

$$\frac{\partial C(0,t)}{\partial t} = \lim_{r \to 0}\left(\frac{\partial^2 C}{\partial r^2} + \frac{2}{r}\frac{\partial C}{\partial r} - \frac{V_{max}C}{C + K_m}\right) = 3\frac{\partial^2 C}{\partial r^2} - \frac{V_{max}C}{C + K_m}, \tag{S25}$$

by use of the Neumann boundary condition in equation (S6) and L'Hôpitals rule. Consequently,

$$\frac{dC_1}{dt} = \frac{3}{\Delta r}\left(\frac{C_2 - 2C_1 + C_0}{\Delta r}\right) - \frac{V_{max}C_1}{C_1 + K_m}. \tag{S26}$$

Thus we need to determine the value of the node C at $i = 0$, i.e. $r = 0 - \Delta r$. In order to do this we apply the Neumann boundary condition in equation (S6).

$$\frac{\partial C_1}{\partial r} = \frac{C_2 - C_0}{2\Delta r} = 0, \qquad\qquad r = 0, \tag{S27}$$

$$\Rightarrow C_0 = C_2. \tag{S28}$$

Therefore,

$$\frac{dC_1}{dt} = \frac{6}{(\Delta r)^2}(C_2 - C_1) - \frac{V_{max}C_1}{C_1 + K_m}, \tag{S29}$$

1.1.1.2   Phase interface boundary

For the interface boundary of the sphere we have a discontinuity and the following equations for the concentrations either side of the boundary:

$$\frac{dC_R}{dt} = \frac{1}{\Delta r}\left(\frac{\tilde{C}_{R+1} - 2C_R + C_{R-1}}{\Delta r} + \frac{\tilde{C}_{R+1} - C_{R-1}}{r}\right) - \frac{V_{max}C_R}{C_R + K_m}, \tag{S30}$$

$$\frac{dC_{R+1}}{dt} = \frac{D}{\Delta r}\left(\frac{C_{R+2} - 2C_{R+1} + \tilde{C}_R}{\Delta r} + \frac{C_{R+2} - \tilde{C}_R}{r}\right), \tag{S31}$$

where special boundary values have been highlighted with accents for extra clarity (note in passive diffusion uninhibited by any membrane permeation, $\tilde{C}_{R+1} = \tilde{C}_R$).

When $i = R$, we define $C_{i+1} = \tilde{C}_{R+1}$ using the equal flux boundary condition (see equation (S8)) and one-sided finite difference approximations and consequently we have

$$D_I \frac{\partial C_I}{\partial r} = D_E \frac{\partial C_E}{\partial r}, \qquad\qquad r = 1, \qquad\qquad \text{(S32)}$$

$$\Rightarrow \frac{\tilde{C}_{R+1} - C_R}{\Delta r} = D \frac{C_{R+1} - \tilde{C}_R}{\Delta r}, \qquad\qquad\qquad \text{(S33)}$$

$$\Rightarrow \tilde{C}_{R+1} = D(C_{R+1} - \tilde{C}_R) + C_R. \qquad\qquad\qquad \text{(S34)}$$

To determine $\tilde{C}_R$ we use the transport boundary condition in equation (S18):

$$D_I \frac{\partial C_I}{\partial r} = Q(C_E - C_I), \qquad\qquad r = 1, \qquad\qquad \text{(S35)}$$

$$\Rightarrow D_I \frac{\tilde{C}_{R+1} - C_R}{\Delta r} = Q(\tilde{C}_R - C_R), \qquad\qquad\qquad \text{(S36)}$$

$$\Rightarrow \tilde{C}_R = \frac{D_I}{Q} \frac{1}{\Delta r}(\tilde{C}_{R+1} - C_R) + C_R. \qquad\qquad\qquad \text{(S37)}$$

Therefore, following substitution into equation (S34),

$$\tilde{C}_{R+1} = \frac{(D - \tilde{Q}\Delta r D + \tilde{Q}\Delta r)C_R + \tilde{Q}\Delta r D C_{R+1}}{\tilde{Q}\Delta r + D}, \qquad\qquad \text{(S38)}$$

where $\tilde{Q} = Q/D_I$ and substituting equation (S38) into equation (S37),

$$\tilde{C}_R = \frac{\tilde{Q}\Delta r C_R + D C_{R+1}}{\tilde{Q}\Delta r + D}. \qquad\qquad \text{(S39)}$$

1.1.1.3 *External boundary*

When $i = N$ we have

$$\frac{dC_N}{dt} = \frac{D}{\Delta r}\left(\frac{C_{N+1} - 2C_N + C_{N-1}}{\Delta r} + \frac{C_{N+1} - C_{N-1}}{r}\right), \qquad\qquad \text{(S40)}$$

and we determine the value of C at $i = N + 1$, i.e. $r = r_{max}$. In order to do this, we apply the Dirichlet boundary condition in equation (S7):

$$C_E = C_{r_{max}} = C_{N+1}, \qquad\qquad r = r_{max}, \qquad\qquad \text{(S41)}$$

Therefore,

$$\frac{dC_N}{dt} = \frac{D}{\Delta r}\left(\frac{C_{r_{max}} - 2C_N + C_{N-1}}{\Delta r} + \frac{C_{r_{max}} - C_{N-1}}{r}\right). \qquad\qquad \text{(S42)}$$

1.1.2 Model simulations

The systems of ODEs derived in section 1.1.1 were numerically integrated using MATLAB R2017b software to illustrate typical solutions (parameters provided in the legend for Figure 1) and a mesh of sufficient resolution to achieve steady state properties ($\frac{1}{r_{res}}\sum_r |C(t_{end},r) - C(0.9t_{end},r)| < 1 \times 10^{-4} C_{r_{max}}$ where r_{res} is the number of spatial steps in the grid and t_{end} is the final time-point value) and consistent internal accuracy ($\max\left(\frac{1}{r_{res}}\sum_r |C_{Ores}(t,r) - C_{Hres}(t,r)|\right) < 1 \times 10^{-4} C_{r_{max}}$ where $C_{Ores}(t,r)$ is the model solution at the original/default resolution (1001x1001 mesh) and $C_{Hres}(t,r)$ is the model solution at an increased mesh resolution where the spatial discretisation is increased 10-fold).

1.2 Carrier-mediated transport

We here reiterate a brief derivation of the simple carrier model used to derive the membrane flux boundary condition for clarity. It is assumed that the drug substrate (external, C_E, or internal, C_I) can reversibly bind to the transporter (facing the exterior, T, or interior, T', of the cell), with first order, mass-action kinetics. The bound transporter complexes are given by the variables CT and CT' for outward and inward facing transporters respectively. It is also assumed that the transporter (bound or unbound) undergoes a conformational change with first order kinetics to change position such that the binding site is facing either the exterior or interior of the cell (see schematic in Fig1A). The above processes are described in the system of ordinary differential equations below:

$$\frac{d[CT]}{dt} = k_{b1+}C_E[T] - k_{b1-}[CT] + k_{c1-}[CT'] - k_{c1+}[CT], \tag{S43}$$

$$\frac{d[CT']}{dt} = k_{b2-}C_I[T'] - k_{b2+}[CT'] + k_{c1+}[CT] - k_{c1-}[CT'], \tag{S44}$$

$$\frac{d[T']}{dt} = k_{b2+}[CT'] - k_{b2-}C_I[T'] + k_{c2-}[T] - k_{c2+}[T'], \tag{S45}$$

$$\frac{d[T]}{dt} = k_{b1-}[CT] - k_{b1+}C_E[T] + k_{c2+}[T'] - k_{c2-}[T], \tag{S46}$$

where k_c terms represent conformational changes, k_b terms represent binding/unbinding and the amount of receptor is conserved, i.e., $CT' + CT + T' + T = T_0$ (constant). The drug substrate flux is given by the difference between interior dissociation of bound substrate and the association of unbound substrate with inward facing receptors (and is equal to the difference between the association of unbound substrate to outward facing receptors and substrate dissociation at the cell exterior). Thus the flux is,

$$J = k_{b2+}[CT'] - k_{b2-}C_I[T'] = k_{b1+}C_E[T] - k_{b1-}[CT], \tag{S47}$$

defined to be positive from outside to inside. It is assumed that the processes of binding and conformational changes are fast relative to the spatiotemporal drug concentration dynamics of the model at the cellular scale. Therefore we can find the steady state flux by setting the left-hand sides of equations (S43)-(S46) equal to 0 and solving to derive the 4 state variables in terms of C_E, C_I and the rate constants, subject to total receptor concentration, T_0. By substitution into equation (S47) we acquire the steady state flux:

$$J = \frac{T_0(C_E - \alpha_1 C_I)}{\alpha_2 + \alpha_3 C_E + \alpha_4 C_I + \alpha_5 C_E C_I}, \qquad (S48)$$

where

$$\alpha_1 = \frac{k_{b1-}k_{c1-}k_{b2-}k_{c2-}}{k_{b1+}k_{c1+}k_{b2+}k_{c2+}}, \qquad (S49)$$

$$\alpha_2 = \frac{(k_{c2+} + k_{c2-})(k_{b1-}k_{c1-} + k_{b1-}k_{b2+} + k_{c1+}k_{b2+})}{k_{b1+}k_{c1+}k_{b2+}k_{c2+}}, \qquad (S50)$$

$$\alpha_3 = \frac{k_{b1+}\left(k_{b2+}(k_{c1+} + k_{c2+}) + k_{c2+}(k_{c1+} + k_{c1-})\right)}{k_{b1+}k_{c1+}k_{b2+}k_{c2+}}, \qquad (S51)$$

$$\alpha_4 = \frac{k_{b2-}\left(k_{c1-}(k_{b1-} + k_{c2-}) + k_{c2-}(k_{b1-} + k_{c1-})\right)}{k_{b1+}k_{c1+}k_{b2+}k_{c2+}}, \qquad (S52)$$

$$\alpha_5 = \frac{k_{b1+}k_{b2-}(k_{c1+} + k_{c1-})}{k_{b1+}k_{c1+}k_{b2+}k_{c2+}}. \qquad (S53)$$

Therefore, we define the following flux boundary condition for the carrier-mediated transport model scenario:

$$D_I \frac{\partial C_I}{\partial r} = \frac{T_0(C_E - \alpha_1 C_I)}{\alpha_2 + \alpha_3 C_E + \alpha_4 C_I + \alpha_5 C_E C_I}, \qquad r = 1. \qquad (S54)$$

1.2.1   Numerical solution

The carrier-mediated transport model was solved numerically using finite difference approximations as before. However, the new boundary condition in equation (S54) required the introduction of modified boundary values in the ODE approximations at the phase interface boundary,

$$\frac{dC_R}{dt} = \frac{1}{\Delta r}\left(\frac{\tilde{C}_{R+1} - 2C_R + C_{R-1}}{\Delta r} + \frac{\tilde{C}_{R+1} - C_{R-1}}{r}\right) - \frac{V_{max}C_R}{C_R + K_m}, \qquad (S55)$$

$$\frac{dC_{R+1}}{dt} = \frac{D}{\Delta r}\left(\frac{C_{R+2} - 2C_{R+1} + \tilde{C}_R}{\Delta r} + \frac{C_{R+2} - \tilde{C}_R}{r}\right), \qquad (S56)$$

With terminology analogous to the passive diffusion model, we use one-sided finite difference approximations and the carrier-mediated flux boundary condition in equation (S54) to determine $\tilde{C}_R$:

$$D_I \frac{\partial C_I}{\partial r} = \frac{T_0(C_E - \alpha_1 C_I)}{\alpha_2 + \alpha_3 C_E + \alpha_4 C_I + \alpha_5 C_E C_I}, \qquad r = 1, \qquad \text{(S57)}$$

$$\Rightarrow \frac{\tilde{C}_{R+1} - C_R}{\Delta r} = \frac{\tilde{T}_0(\tilde{C}_R - \alpha_1 C_R)}{\alpha_2 + \alpha_3 \tilde{C}_R + \alpha_4 C_R + \alpha_5 \tilde{C}_R C_R}, \qquad \text{(S58)}$$

$$\Rightarrow \tilde{C}_R = \frac{(C_R - \tilde{C}_{R+1})(\alpha_2 + \alpha_4 C_R) - \Delta r \tilde{T}_0 \alpha_1 C_R}{(\tilde{C}_{R+1} - C_R)(\alpha_3 + \alpha_5 C_R) - \Delta r \tilde{T}_0}, \qquad \text{(S59)}$$

where $\tilde{T}_0 = T_0/D_I$. Therefore, following substitution into the equal flux equation (S34), we can derive a quadratic equation for $\tilde{C}_{R+1}$,

$$\begin{aligned}
&\tilde{C}_{R+1}^2(\alpha_3 + \alpha_5 C_R) \\
&-\tilde{C}_{R+1}\Big(2C_R(\alpha_3 + \alpha_5 C_R) + \Delta r \tilde{T}_0 + DC_{R+1}(\alpha_3 + \alpha_5 C_R) + D(\alpha_2 + \alpha_4 C_R)\Big) \\
&+C_R\big((DC_{R+1} + C_R)(\alpha_3 + \alpha_5 C_R) + D(\alpha_2 + \alpha_4 C_R)\big) - \Delta r \tilde{T}_0(D\alpha_1 C_R - C_R - DC_{R+1}) \\
&= 0,
\end{aligned} \qquad \text{(S60)}$$

and numerically integrate the full system of ODEs as described in section 0.

2　Parameterisation of passive diffusion

2.1　*Diffusion of small molecule drugs*

From a sample data base of 321 drugs, we identified several important physicochemical properties including molecular weight and density (Kyffin, 2018). These values allowed us to formulate an estimated range of likely diffusion coefficients for a wide range of drugs with a physically accurate range of weights and densities by employing the Stokes-Einstein equation describing the diffusion of spherical particles through a liquid with low Reynolds number,

$$D = \frac{k_B T}{6\pi\mu r}, \tag{S61}$$

where k_B is Boltzmann's constant, T represents temperature (assumed to be the physiological value, 310.15 K), μ is viscosity (assigned as 6.913×10^{-4} kg m^{-1} s^{-1}, the dynamic viscosity of water at 310.15 K) and r is the particle radius (m). To calculate the radius, we assume drugs can be represented spherically and use MW and density (ρ) data:

$$r = \sqrt[3]{\frac{3}{4\pi} \frac{MW}{\rho} \frac{1}{6.02 \times 10^{23}}} \ \text{m}. \tag{S62}$$

By implementing the formulae in (S61) and (S62) for the drug data base (MW ~100-1,200; density ~0.6-2.6 g/m^3), we were able to identify a feasible diffusion coefficient range of approximately 5×10^{-10} to 1×10^{-9} m^2/s.

2.2　*Permeability as a function of lipophilicity*

Menochet et al. (2012a, 2012b) discovered a log-linear relationship between lipophilicity (LogD$_{7.4}$) and "passive diffusion clearance" (P_{diff}) for xenobiotic uptake in human and rat hepatocytes. LogD$_{7.4}$ can be defined as a partition coefficient measure of lipophilicity at a physiologically relevant pH (pH = 7.4). For example, Menochet et al. derived the following relationship for human hepatocytes:

$$\log P_{diff} = 0.6316 \times \text{LogD}_{7.4} - 0.3143. \tag{S63}$$

In the study, the uptake rate is defined as the slope of the linear regression of the intracellular concentration-versus-time plot after 2 minutes at 4 °C (dimensions: [A]/10^6 cells·1/[T], [A] = amount units, [T] = time units). At early times, we assume that passive diffusion can be represented by the following system where the rate constant k_{in} represents the transport of drug into the cell:

$$\frac{dA_{cell}}{dt} = k_{in}V_{med}C_0 \tag{S64}$$

where A_{cell} is the amount of drug (units of moles) in the cellular compartment (expressed per 10^6 cells) and C_0 is the substrate or media concentration (moles dissolved in V_{med} = 400 μL of media in the

Menochet et al. study), which we assume to be an approximate constant external supply at early times, i.e., equivalent to dose concentration. The passive diffusion clearance, P_{diff}, is defined as the slope of the uptake rate against concentration,

$$\text{Uptake rate} = P_{diff}C_{out}\,, \tag{S65}$$

for media substrate C_{out} and dimensions,

$$\frac{[A]}{10^6 \text{ cells} \cdot [T]} = \frac{[V]}{10^6 \text{ cells} \cdot [T]} \cdot \frac{[A]}{[V]}\,, \tag{S66}$$

where [V] = volume units. By comparison with equation (S64), at early times, we have

$$\text{Uptake rate} = P_{diff}C_0 = \frac{dA_{cell}}{dt} = k_{in}V_{med}C_0\,, \tag{S67}$$

$$\Rightarrow P_{diff} = k_{in}V_{med}\,, \tag{S68}$$

where P_{diff} has units of μL/min/10^6 cells in the Menochet et al. study.

In order to translate this uptake-related parameter into our spatial model we must derive the total intracellular-amount dynamics by integrating over the cell volume. At early times in low temperatures (no metabolism) we have the following system for drug concentration and transport into a single cell:

$$\frac{\partial C}{\partial t} = \begin{cases} \dfrac{\partial C_{cell}}{\partial t} = \nabla \cdot (D_{cell}\nabla C_{cell}) & r \leq R \\[3mm] \dfrac{\partial C_{out}}{\partial t} = \nabla \cdot (D_{out}\nabla C_{out}) & r > R \end{cases} \tag{S69}$$

We can define the amount of intracellular drug in the cell as follows:

$$A_{cell} = \int_{V_{cell}} C_{cell}\, dV = 4\pi \int_0^R C_{cell}\, r^2 dr\,. \tag{S70}$$

To define the total uptake rate for the entire cell we integrate the intracellular concentration dynamics with respect to the volume of the cell,

$$\frac{dA_{cell}}{dt} = \int_{V_{cell}} \frac{\partial C_{cell}}{\partial t}\, dV = \int_{V_{cell}} \nabla \cdot (D_{cell}\nabla C_{cell})\, dV = \int_S D_{cell}\nabla C_{cell} \cdot \mathbf{n}\, dS\,, \tag{S71}$$

by the divergence theorem for surface, S, i.e. the surface area of the cell of radius R. It follows that

$$\int_S D_{cell}\nabla C_{cell} \cdot \mathbf{n}\, dS = 4\pi R^2 D_{cell} \left.\frac{\partial C_{cell}}{\partial r}\right|_{r=R}\,. \tag{S72}$$

We have the following boundary condition (see equation (S18)) at $r = R$,

$$D_{cell}\frac{\partial C_{cell}}{\partial r} = Q(C_{out} - C_{cell}) \approx QC_0, \tag{S73}$$

at early times ($C_{out} \approx C_0$ and $C_{cell} \approx 0$) where Q represents the permeability coefficient in units of [L]/[T] where [L] = length units. Substituting this result back into equation (S72), for a single cell, we obtain,

$$\frac{dA_{cell}}{dt} = 4\pi R^2 Q C_0 = \frac{P_{diff}C_0}{10^6}. \tag{S74}$$

Therefore,

$$\frac{P_{diff}C_0}{10^6} = 4\pi R^2 Q C_0 , \tag{S75}$$

and we can derive the permeability coefficient for our model, Q, as a function of P_{diff}, itself a function of the physicochemical property LogD$_{7.4}$, and the radius of the cell, R:

$$Q = \frac{P_{diff}}{4\pi R^2} = \frac{1}{10^6}\frac{10^{(0.6316 \times \text{LogD}_{7.4} - 0.3143)}}{4\pi R^2}. \tag{S76}$$

3   Translating the multiscale model to a simple continuum model

3.1   *Optimisation of effective parameters for the simple continuum model*

The average steady state profiles for the full, multiscale models were acquired by extracting 8 1D radial profiles from cross-sections through the centre of the spheroid slice corresponding to the lines $y = 0$, $x = 0$, $y = x$ and $y = -x$ and calculating the mean. This method was initially validated by comparing the simple continuum model with the average radial profile of the full model with no intercellular space/zero porosity (i.e., the model used in Figure 4A), both using the default parameter set, i.e., $D_I^{Eff} = D_I$ and $Q^{Eff} = Q$ (see Figure S2A). In order to optimise the effective parameter values required to fit the simple continuum model to the cell-based models with inclusion of intercellular space, D_I^{Eff} and Q^{Eff} were varied by up to three orders of magnitude either side of the default dimensional value (e.g., $D_I^{Eff} = [1 \times 10^{-3}, 1 \times 10^{3}] \times D_I$ discretised over a log-scale for 51 points distributed within the interval) and the minimum residual error at steady state between the continuum and cell-based models was identified according to the following formula:

$$Error = \sum_i \left| \frac{C_{cont}(r_i, t^*) - \bar{C}_{cells}(r_i, t^*)}{\bar{C}_{cells}(r_i, t^*)} \right|, \tag{S77}$$

where C_{cont} represents the continuum model output, $\bar{C}_{cells}$ represents the average cell-based model output, r is radial distance (discretised at every μm from 0 to 750 μm, $i = 1:751$) and t^* indicates the

13

steady state. This process was repeated for both intercellular space geometries (wide and narrow) and a range of feasible permeability coefficients (corresponding to $LogD_{7.4}$ = 1, 2, 3, 4, 5).
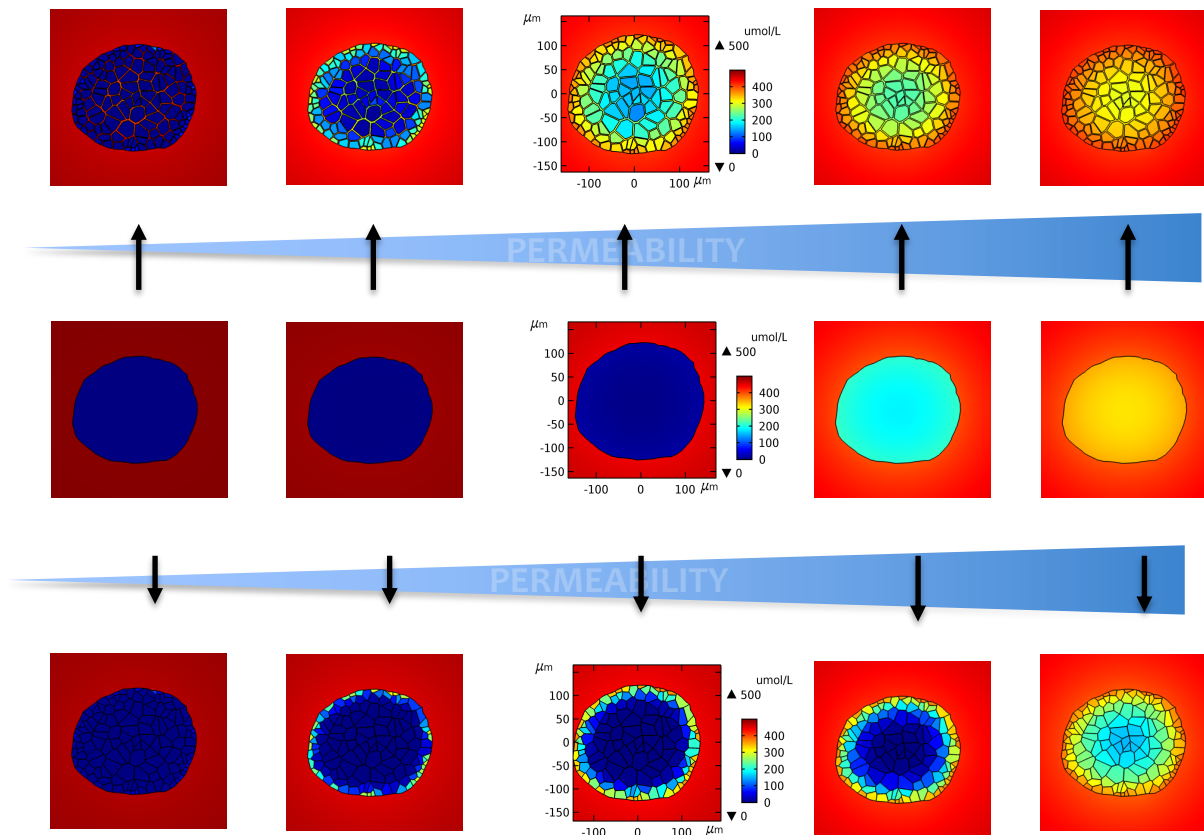

Figure S1: **Spatial distribution of drug concentration pre-optimisation.** The 2D spatial distribution of drug concentration at steady state for a range of permeabilities and intercellular space values are plotted. Permeability increases from left to right ($LogD_{7.4}$ = 1, 2, 3, 4, 5). (Top row): Spatial plots for the wide intercellular space geometry. (Middle row): Spatial plots for zero intercellular space, analogous to the simple continuum model pre-optimisation. (Bottom row): Spatial plots for the narrow intercellular space geometry. All models solutions are generated using the default parameter set.
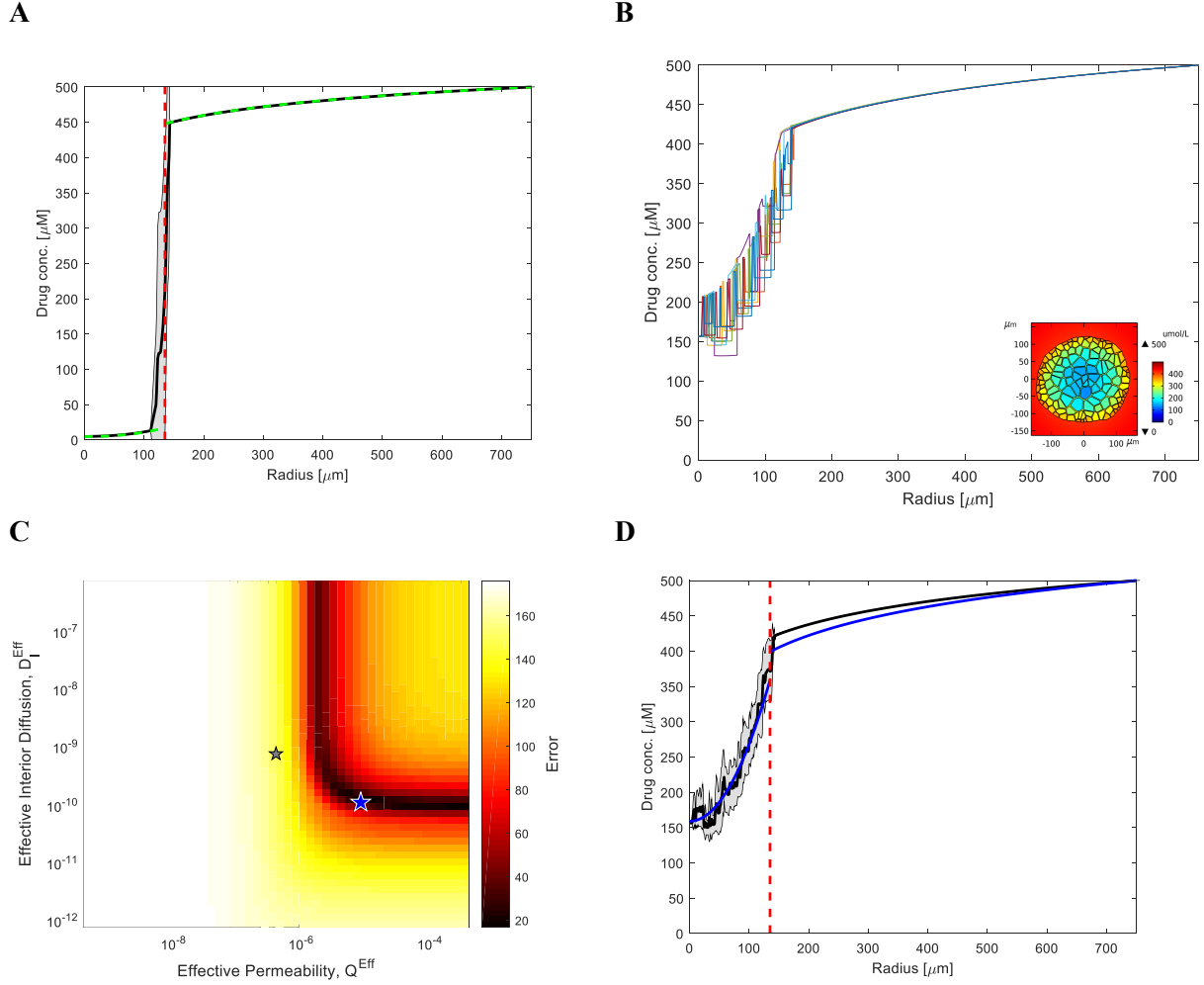
Figure S2: **Parameter optimisation for continuum model.** (A): Comparison of the "continuum model" output (green-dashed line, from equations 16-19 in the main manuscript) with the average radial profile for the "cell-based model" (black-solid line with grey standard deviation) with zero intercellular space (e.g., Figure 4A) at steady state using the same parameters (i.e., $D_I^{Eff} = D_I$ and $Q^{Eff} = Q$) The vertical red-dashed line indicates the spheroid boundary in the continuum model. (B): Example of 8 radial profiles used to calculate average behaviour of the cell-based model (default parameters at $LogD_{7.4} = 3$ steady state). The 2D spatial distribution is also indicated (inset). (C): Example parameter sweep output representing error outputs (equation (S77)) for wide intercellular space, $LogD_{7.4} = 3$. The original default parameters from the dimensional cell based model are indicated by the grey star. The minimum error representing optimal effective parameters is indicated by the blue star. (D): The continuum model steady state output (blue line) produced using the optimal effective parameters (i.e., blue star, (C)) is plotted against the average radial output of the cell-based model (black-solid line with grey standard deviation).

For plotting purposes in Figure 5F, cell-based models were compared with the continuum model by making use of the standard R^2 error metric:

$$R^2 = 1 - \frac{\sum_i \left| \frac{\bar{C}_{cells}(r_i, t^*) - C_{cont}(r_i, t^*)}{C_{cont}(r_i, t^*)} \right|}{\sum_i \left| \frac{\text{mean}(C_{cont}(r_i, t^*)) - C_{cont}(r_i, t^*)}{C_{cont}(r_i, t^*)} \right|} . \tag{S78}$$

References

Kyffin J A (2018). <u>Establishing species-specific 3D liver microtissues for repeat dose toxicology and advancing in vitro to in vivo translation through computational modelling</u> PhD Thesis, Liverpool John Moores University.

Ménochet K, Kenworthy K E, Houston J B and Galetin A (2012a) Use of mechanistic modeling to assess interindividual variability and interspecies differences in active uptake in human and rat hepatocytes. *Drug Metabolism and Disposition* 40: 1744-1756.

Ménochet K, Kenworthy K E, Houston J B and Galetin A (2012b) Simultaneous assessment of uptake and metabolism in rat hepatocytes: a comprehensive mechanistic model. *Journal of Pharmacology and Experimental Therapeutics* 341: 2-15.